The NORSEWInD numerical wind atlas for the South Baltic

Hahmann, Andrea N.; Lange, Julia; Pena Diaz, Alfredo; Hasager, Charlotte Bay

Publication date:
2012

Document Version
Publisher's PDF, also known as Version of record

The NORSEWInD numerical wind atlas for the South Baltic

DTU Wind Energy E-Report

Andrea N. Hahmann, Julia Lange, Alfredo Peña, and Charlotte B. Hasager

DTU Wind Energy-E-Report-0011(EN)
November 2012

DTU Wind Energy
Department of Wind Energy

DTU Wind Energy-E-Report-0011(EN)

The NORSEWInD numerical wind atlas for the South Baltic

Andrea N. Hahmann, Julia Lange, Alfredo Peña and Charlotte B. Hasager

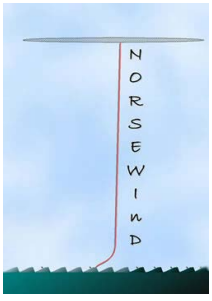

DTU Wind Energy
Department of Wind Energy

**DTU Wind Energy, Risø Campus,
Technical University of Denmark, Roskilde, Denmark**

November 2012

Author: Andrea N. Hahmann, Julia Lange, Alfredo Peña and Charlotte B. Hasager
Title: The NORSEWInD numerical wind atlas for the South Baltic
Department: DTU Wind Energy

DTU Wind Energy-E-Report-0011(EN)
November 27, 2012

ISSN:978-87-92896-17-9
ISBN:978-87-92896-17-9

Abstract (max. 2000 char)

This document reports on the method used to create a numerical wind atlas for the South Baltic under the EU-FP7 project "Northern Seas Wind Index Database" also known as NORSEWInD. The wind atlas is created from the output of climate-type simulations with the Weather, Research, and Forecasting (WRF) model.
The report is divided into three main parts. In the first part, we examine the sensitivity of the mean wind speed and planetary boundary layer stability parameters to details of the model simulations. In the second part, we validate the wind atlas against wind observations at several mast and lidar sites. Generalized wind climates derived from the WRF simulations are also validated against generalized wind climates for sites within Denmark. In the third part, we provide maps of the wind climatology and stability conditions in the South Baltic sea as derived from the winds and stability parameters of the WRF simulations.

Contract no:
TREN-FP7EN-219048

Project no:
43013

Sponsorship:
FP7

Cover:

Pages: 52
Tables: 5
Figures: 36
References: 31

Technical University of Denmark
Frederiksborgvej 399
4000 Roskilde
Denmark
Tel. +4546775024
bcar@dtu.dk
www.vindenergi.dk

Contents

1 Introduction

In this report we introduce the method used and present the main results of the production of the South Baltic wind atlas for the EU-FP7 project "Northern Seas Wind Index Database" also known as NORSEWInD. The NORSEWInD project was designed to deliver high quality hub-height wind atlases based on physical data for the Baltic, Irish and North Seas. The Baltic Sea section of the wind atlas was produced at DTU Wind Energy, while the North and Irish wind atlases were produced by our partners in the project at Kjeller Vindteknikk.

Since the project focused on the analysis of the wind shear offshore, many of the fields produced by the wind atlas also focus on this quantity and related parameters, such as wind shear parameter and atmospheric stability. An attempt was made to standardize the computation of various parameters in the North, Irish and Baltic wind atlases. However, this is not always possible because different versions of the mesoscale model with different parameterizations were used in the calculations.

This report is structured in the following manner. In Section 2 we define the modeling details of the project: model setup and the choice of model parameterizations. In Section 3 we describe the methods used in the post-processing of the raw model wind fields: long-term correction, and generalization of the mesoscale model results. In Section 4 we present the results of the sensitivity of the model simulations to various parameters, including driving reanalysis and sea surface temperatures. Verification of the wind climatologies derived from the WRF simulations against data from various sites is done in Section 5. Here we also validate the generalized wind climate derived from the model output and the observations. In Section 6 we present plots of the wind atlas parameters. Conclusions are presented in the last section of the report (Section 7).

2 Background

2.1 Model Description

The Weather, Research and Forecasting (WRF) Model (Skamarock et al., 2008) is a mesoscale numerical weather prediction system designed to serve both operational forecasting and atmospheric research needs. The model was developed and continues to be updated by a consortium of institutions in the USA lead by the National Center for Atmospheric Research (NCAR). The WRF model is suitable for a broad spectrum of applications across scales ranging from meters to thousands of kilometers. The WRF models allows researchers to conduct simulations reflecting either real data or idealized configurations. WRF provides operational forecasting with a model that is flexible and efficient computationally, while offering the advances in physics, numerics, and data assimilation contributed by the research community.

Although designed primarily for weather forecasting applications, ease of use and quality has brought the WRF model to be the model of choice for downscaling in wind energy applications. This model was used in wind-related studies concerning: wind shear in the North Sea (Peña and Hahmann, 2012) and over Denmark (Draxl et al., 2012), organized convection in the North Sea (Vincent et al., 2012), low-level jets in the central USA (Storm et al., 2009), wind climate over complex terrain (Horvath et al., 2012), gravity waves (Larsén et al., 2012), extreme winds (Larsén et al., 2012), among others.

2.2 WRF model setup

For generating wind climatologies over the South Baltic we used version 3.2.1 of the Advanced Research WRF (ARW-WRF) model. Details of this model can be found in Skamarock et al. (2008) and Wang et al. (2010). Two main simulations are used for the generation of the atlas: a relatively long (2006–2011) simulation using a grid with 5 km horizontal spacing, which from now on we will refer as "control", and a much longer (1999–2011) simulation using a coarser horizontal grid spacing (15 km), which we will refer as "reference". The reference simulation was used only in the long-term correction of the wind atlas and the estimation of

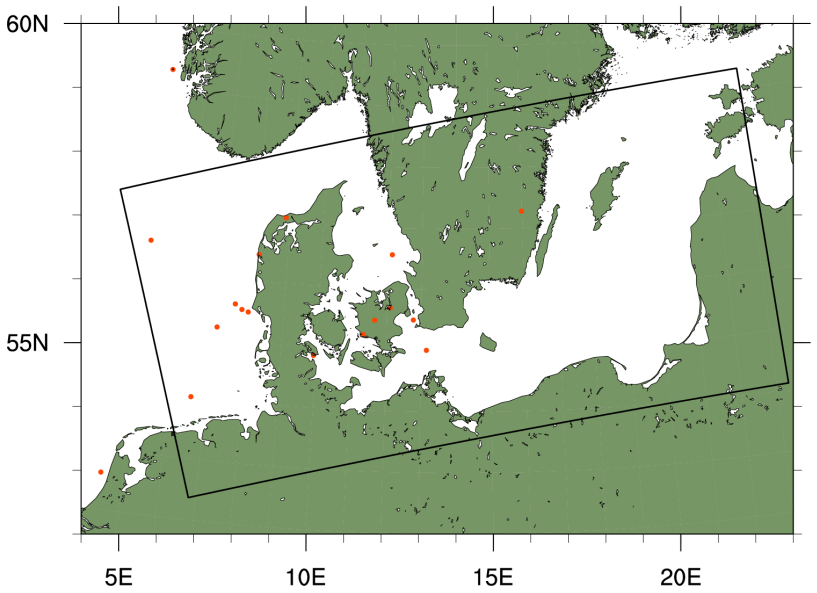

Figure 1: Location of the WRF inner model domain (D2) and some of the meteorological masts (red dots) used in the verification of the results.

interannual variability in mean annual wind speed. Both model setups are briefly described below.

Control simulation

The model setup for the control simulation is described in Table 1, except for the various surface, boundary layer, and land surface parameterizations used in the sensitivity experiments that will be presented in section 4. It is worth noting that the grid used was rotated to better cover the region of interest as shown in Figure 1. Figures 2 and 3 show the terrain elevation and land use used in the simulations. The terrain is derived from USGS (United States Geological Service) 30" (about 1 km) spatial resolution data. The landuse is derived from Moderate Resolution Imaging Spectroradiometer (MODIS) at 30" with 20 categories.

The choice of model setup and parameterizations is based on our previous experience using WRF for wind forecasting (Hahmann and Peña, 2010; Draxl et al., 2012) and wind atlas

Table 1: Summary of model and system setup and physical parameterizations used in the control WRF simulations.

Model setup:
WRF (ARW) Version 3.2.1.
Mother domain (D1; 102 $\times$ 70 grid points) with 15 km grid spacing; 1 nested domain (D2; 205 $\times$ 106) using 5 km horizontal grid spacing on a polar stereographic projection (see Fig. 1).
41 vertical levels with model top at 50 hPa; 9 of these levels are placed within 1000 m of the surface; The first 6 levels are located approximately at: 14, 43, 72, 100, 129 and 190 m.
MODIS land-cover classification of the International Geosphere-Biosphere Programme.
Simulation setup:
Initial, boundary conditions, and fields for grid nudging come from the European Centre for Medium Range Forecast (ECMWF) ERA-Interim Reanalysis (Dee et al., 2011) at 0.7° $\times$ 0.7° resolution.
Runs are started (cold start) at 00:00 UTC every 10 days and are integrated for 11 days, the first 24 hours of each simulation are disregarded.
Sea surface temperature (SST) and sea-ice fractions come from the dataset produced at USA NOAA/NCEP at 1/12° $\times$ 1/12° resolution (Gemmill et al., 2007) and are updated daily.
Model output: hourly (lowest 11 vertical levels), wind speeds at 3 vertical levels every 10 minutes. Time step in most simulations: 90 seconds.
One-way nested domains; 5 grid point nudging zone.
Grid nudging on D1 only and above level 10; nudging coefficient 0.0003 s^{-1} for wind, temperature and specific humidity.
Physical parameterizations:
Precipitation: Thompson graupel scheme (option 8), Kain-Fritsch cumulus parameterization (option 1)
Radiation: RRTM scheme for longwave (option 1); Dudhia scheme for shortwave (option 1)
PBL and land surface: Mellor-Yamada-Janjic scheme (Mellor and Yamada, 1982) (option 2), Eta similarity (option 2) surface-layer scheme, and Noah Land Surface Model (option 2).
Diffusion: Simple diffusion (option 1); 2D deformation (option 4); 6th order positive definite numerical diffusion (option 2); rates of 0.06, 0.08, for D1 and D2, respectively; no vertical damping.
Positive definite advection of moisture and scalars.

studies (Peña et al., 2011; Peña and Hahmann, 2012).

Reference simulation

For long-term correction of the wind speeds a control simulation from a previous WRF simulation study was used. The simulations were carried out using the method of Hahmann et al. (2010) and are described in Peña and Hahmann (2012).

Initial and boundary conditions and the gridded fields used in the nudging are taken from the USA National Oceanic and Atmospheric Administration (NOAA), National Centers for Environmental Predictions (NCEP) Reanalysis II (Kanamitsu et al., 2002) at 2.5° × 2.5° grid spacing. The Sea Surface Temperatures (SST) are obtained at 0.25° × 0.25° horizontal grid spacing and temporal resolution of 1 day are interpolated to the model grid. The simulation covers the period from 1 January 1999 to 31 December 2011 with hourly outputs. The model configuration is similar to that of the control simulation with 41 vertical levels with the model top at 50 hPa. The outer domain has a horizontal grid spacing of 45 km that covers all

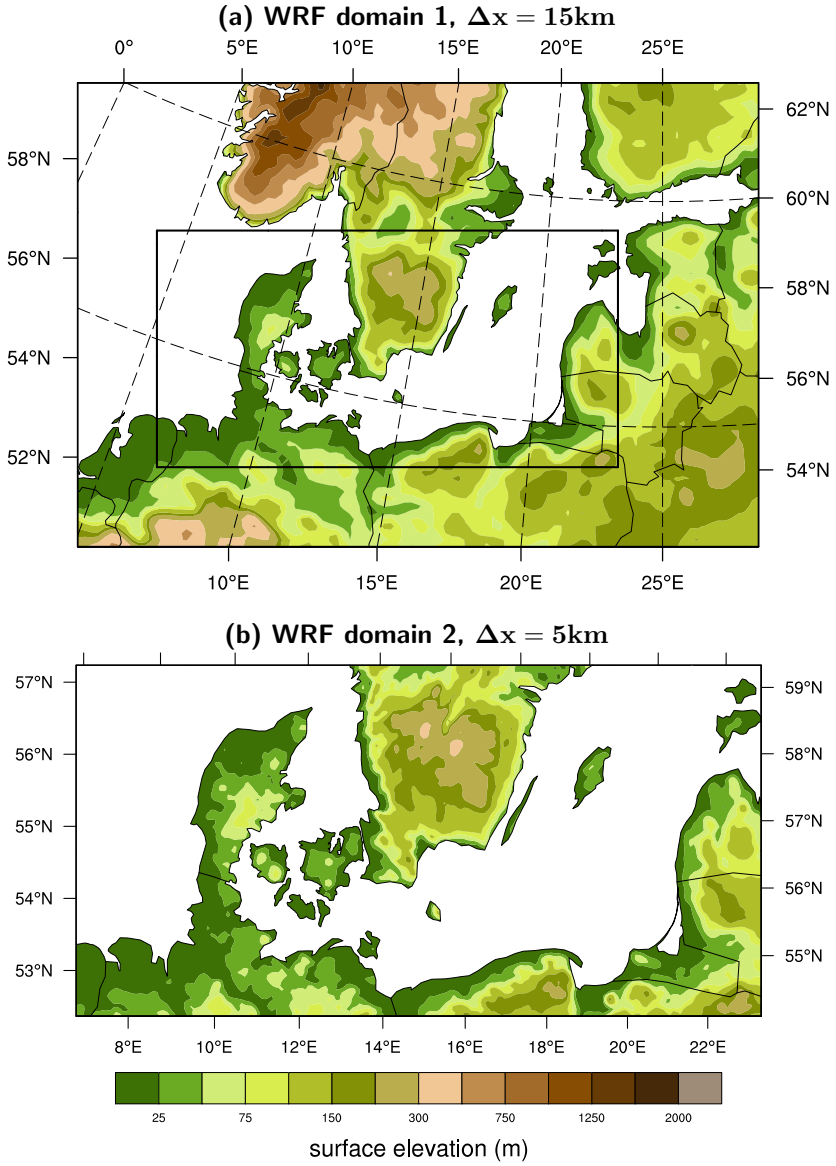

Figure 2: Terrain elevation (in m) used in the WRF simulations for: (a) Domain 1, $\Delta x = 15$ km; and (b) Domain 2, $\Delta x = 5$ km.

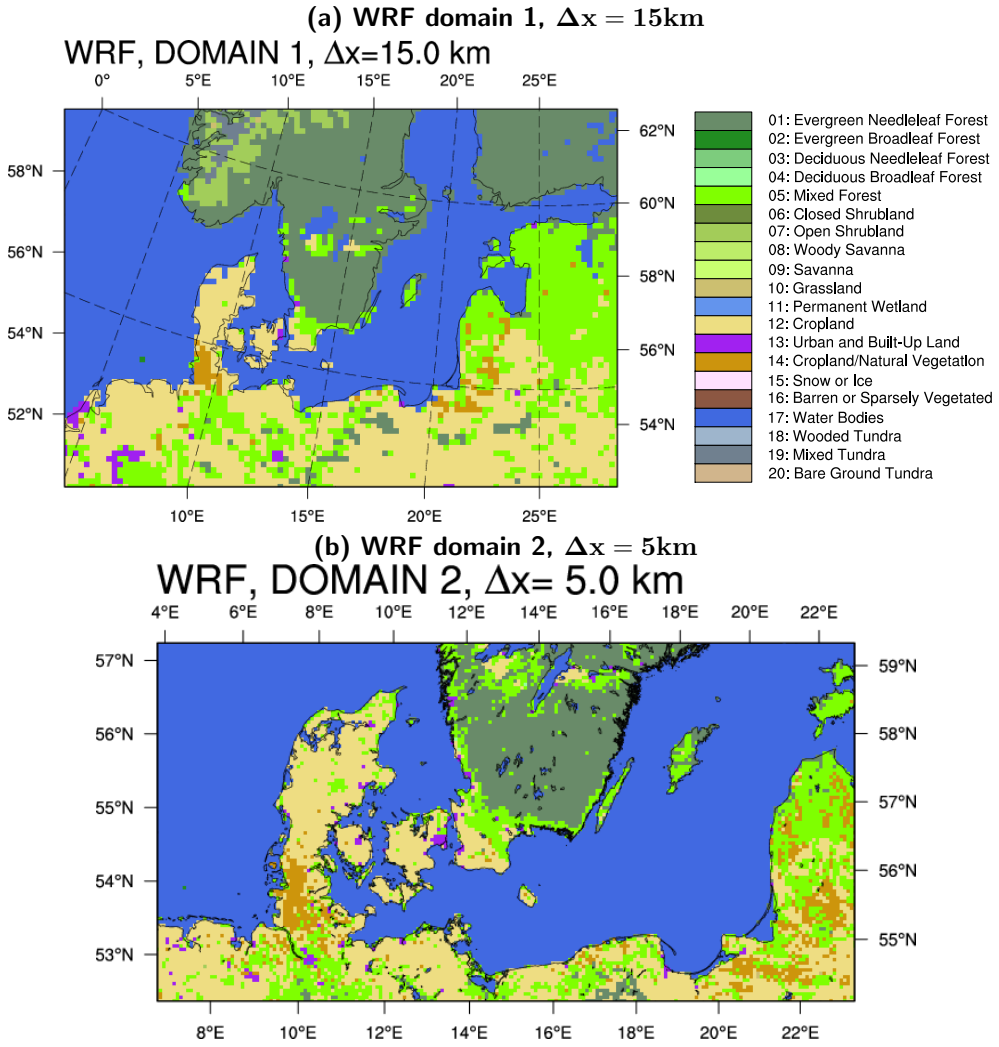

Figure 3: Landuse classes used in the WRF simulations for: (a) Domain 1, $\Delta x = 15$ km; and (b) Domain 2, $\Delta x = 5$ km.

of Europe, and the nested inner domain 15 km that extends from southern Scandinavia to the British Isles. Most physical parameterizations in this simulation are as in the control simulation except that we use the Yonsei University PBL scheme (Hong et al., 2006) and the MM5 surface layer-scheme.

3 Methods

3.1 Long-term adjustment

To reduce the uncertainty associated with climate variability in the estimation of wind resources, a statistical relationship is typically established between a monitoring site and one or more reference stations using a technique known as Measure-Correlate-Predict (MCP). The method is usually applied to a single monitoring site and one or more reference stations or grid points from atmospheric reanalysis.

In this study we extended the MCP method to two spatial dimensions by using output from high- and low-resolution mesoscale modeling. In this manner, the wind maps generated for a relatively short time period with a high-resolution (HR) simulation can be extended in time to include interannual variations in wind resources from a low-resolution (LR) simulation. We use the simulation described in Section 2.2 as the "monitoring" high-resolution simulation (2006–2011) and the "reference" wind speed was provided by a coarser resolution simulation (1999–2011), described in section 2.2. We use the hourly time series of wind speed at 100 m from both simulations for this purpose.

The annual mean long-term corrected wind speed at grid point (i, j) in the HR grid is given by

$$\overline{U}_{HR}^{ij} = b^{ij}\overline{U}_{LR}^{ij} + a^{ij}, \tag{1}$$

where $\overline{U}_{LR}^{ij}$ is the time-average wind speed in the LR simulation grid point closest to the HR grid. The constants a^{ij} and b^{ij} represent the offset and time correlation between U_{HR}^{ij} and U_{LR}^{ij}, respectively. Figure 4 shows such correlation calculated for the period 1 January 2006 to 31 December 2011. Correlations vary between about 0.7 and 0.8, with generally lower correlations downstream from land masses in the dominant wind direction.

The annual mean long-term wind speed computed using Eq. 1 is shown in Figure 5 and also its difference from the simpler annual mean time-averaged wind speed for the period 1 Jan 2006 to 31 Dec 2011. Therefore, applying the long-term correction has reduced the annual mean wind speed in this region by an average of $\leq 1\%$.

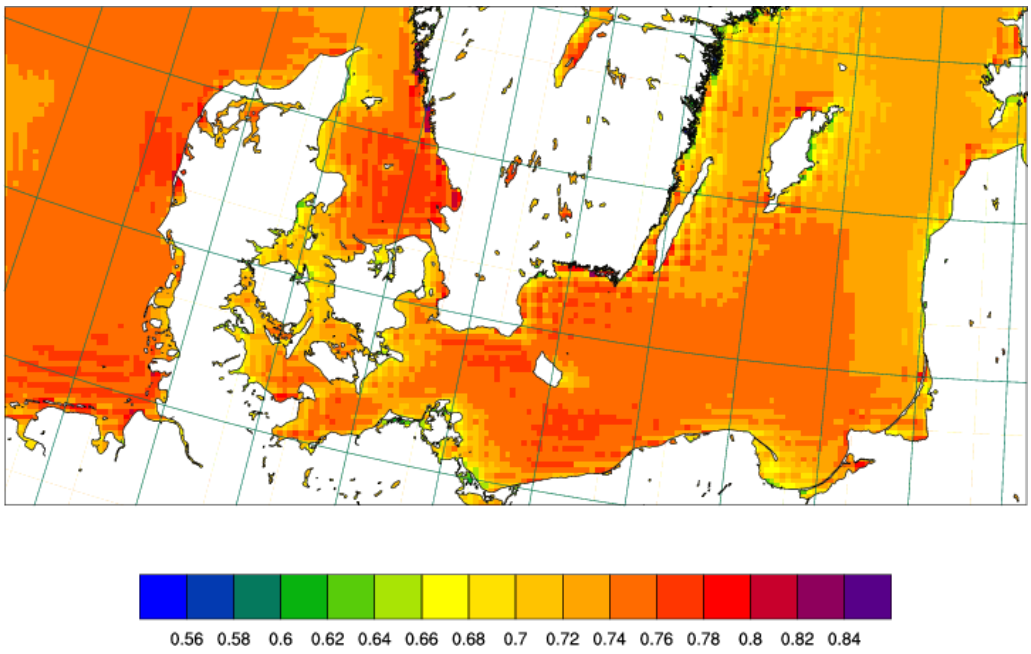

Figure 4: Linear correlation between the hourly time series of wind speed at 100 meters in the HR grid and LR grid for the period 1 January 2006 to 31 December 2011.

(a) Annual mean wind speed ($m\,s^{-1}$) at 100 m.

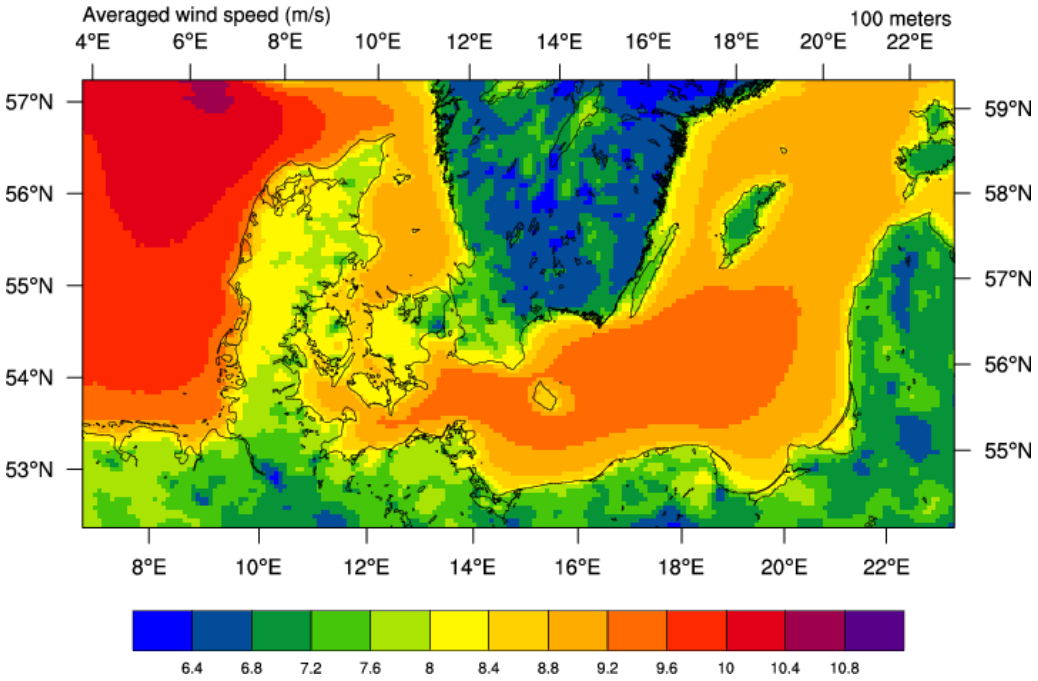

(b) Difference in annual mean wind speed at 100 m (%)

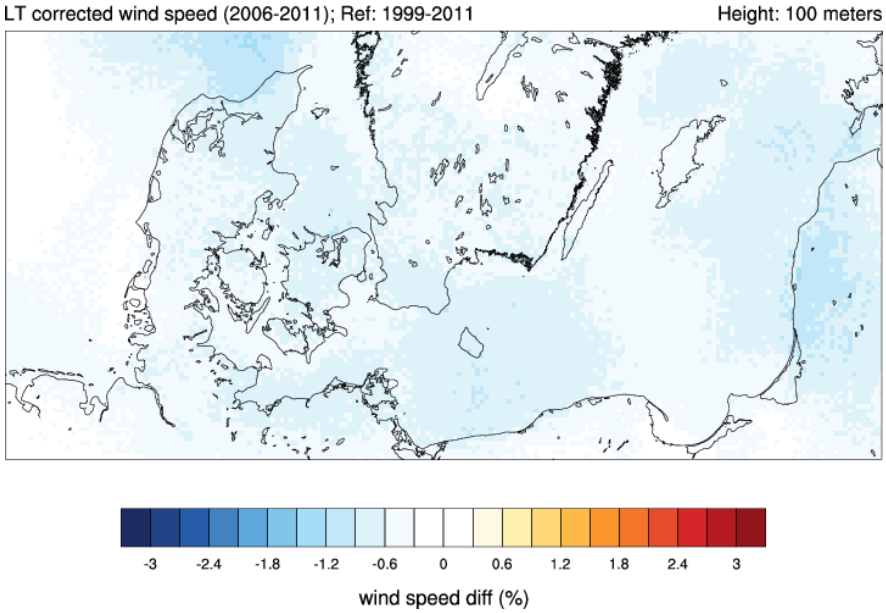

Figure 5: Long-term corrected wind speed (top; $m\,s^{-1}$) and difference between long-term corrected and simple time-average wind speed (bottom; %) for the period 1 January 2006 to 31 December 2011 at 100 m.

It is important to emphasize that just as with point based MCP methods, the period chosen for the concurrent simulation must contain to high degree the variety of synoptic states that occur in the region of interest. Only if these states are included will the MCP be representative. In case the simulation is too short, not all possible synoptic states will be represented and thus the long-term correction will be incomplete.

An example of a too short simulation is presented in Figure 6. The figure shows the difference in long-term corrected wind speed (%) obtained from using different periods and lengths of concurrent simulations. In this case using the period of one year (May 2006–April

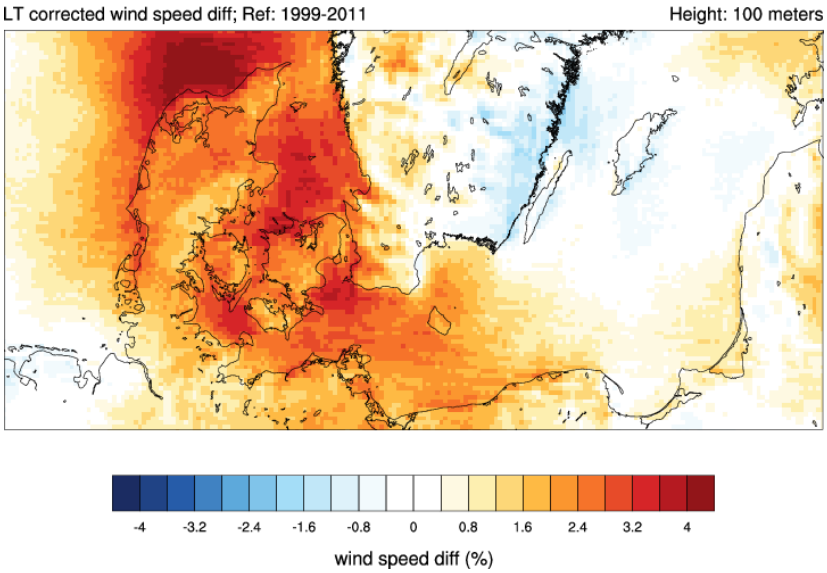

Figure 6: Difference in long-term corrected wind speed (%) at 100 m when using a different length of concurrent simulations: estimate using May 2006–April 2007 minus that using January 2006–December 2011. The reference simulation is the same covering the period 1999–2011.

2007) resulted in an estimate of wind speed up to 5% larger than if using a longer period (January 2006–December 2011). In other words, the period May 2006–April 2007 was very windy and thus unrepresentative of the longer-period wind climate.

The exercise in Figure 6 cannot be done in every wind atlas study. However, it should be possible to study the representativeness of the concurrent period in relation to, for example, the wind speed climatology of a reanalysis dataset. Such a study was carried out by Hagemann (2008) in his wind atlas for South Africa. Another possibility is to choose a sample of representative days in the concurrent simulation such as proposed by Rife et al. (2012) instead of a continuous time period.

3.2 Weibull distribution fit

The frequency distribution of the horizontal wind speed often can be reasonably well described by the Weibull distribution function (Tuller and Brett, 1984):

$$f(u) = \frac{k}{A}\left(\frac{u}{A}\right)^{k-1} \exp\left[-\left(\frac{u}{A}\right)^{k}\right], \tag{2}$$

where $f(u)$ is the frequency of occurrence of the wind speed u. In the Weibull distribution the scale parameter A has wind speed units and is proportional to the average wind speed calculated from the entire distribution. The shape parameter $k(\geq 1)$ describes the skewness of the distribution function. For typical wind speed distributions, the k-parameter has values in the range of 2 to 3.

From the values of A and k, the mean wind speed M ($\mathrm{m\,s^{-1}}$) and mean power density E ($\mathrm{W\,m^{-2}}$) in the wind can be calculated from:

$$M = A\Gamma\left(1+\frac{1}{k}\right) \tag{3}$$

$$E = \frac{1}{2}\rho A^3 \cdot \Gamma\left(1+\frac{3}{k}\right) \tag{4}$$

where ρ is the mean density of the air and Γ is the gamma function. We use the moment fitting method as used in the Wind Atlas Analysis and Application Program (WAsP) for

estimating the Weibull parameters. The method is described in detail in Troen and Petersen (1989). Basically this method estimates A and k to fit the power density in the time series instead of the mean wind speed.

3.3 Stability and wind shear parameters

Several measures of atmospheric stability and wind shear are presented in this atlas. We define them below.

Wind shear parameter

We use the power exponent parameter α defined from the power law:

$$u(z) = u_r \left(\frac{z}{z_r} \right)^{\alpha}, \tag{5}$$

where u_r and z_r are a reference wind speed and height. For a given set of heights, the value of α depends on atmospheric stability and roughness length. Alternatively, Eq. 5 can be rewritten as

$$\alpha = \frac{du}{dz} \frac{z}{u}. \tag{6}$$

In order to minimize the effect of model vertical resolution in the calculation of α we adopted the following method. First, the simulated vertical wind profile is approximated by a polynomial function:

$$u(z) = a_0 + a_1 \ln z + a_2 (\ln z)^2 \tag{7}$$

using a traditional least squares fit. From this equation, α is then

$$\alpha = \frac{z}{u} \frac{a_1 + 2a_2 \ln z}{z}. \tag{8}$$

We use, $z = 100\,\mathrm{m}$ and u at 100 m, interpolated from the model levels. The polynomial fit uses values at levels 2–5, approximately from 43 to 130 meters in the control simulation.

Obukhov length

The Obukhov length, L, can be estimated as

$$L = -\frac{u_*^3 T}{\kappa\, g\, \overline{w'\theta'_v}}, \tag{9}$$

where T is the mean air temperature, and $\overline{w'\theta'_v}$ is the kinematic virtual heat flux. The Obukhov length is proportional to the height above the surface at which buoyant factors dominate over shear production of turbulence (Stull, 1988). In the WRF model, L is computed within the WRF surface-layer scheme.

Following Gryning et al. (2007), we classify the surface layer stability according to: $1/L < -0.005\,\mathrm{m}^{-1}$ (unstable); $-0.005\,\mathrm{m}^{-1} < 1/L < 0.005\,\mathrm{m}^{-1}$ (neutral); $0.005\,\mathrm{m}^{-1} < L < 0.02\,\mathrm{m}^{-1}$ (stable); and $1/L > 0.02\,\mathrm{m}^{-1}$ (very stable).

Static stability

In addition to the Obukhov length, we also present a measure of static stability given by the vertical gradient of potential temperature, $\partial\theta/\partial z$. We use potential temperature and heights at the first and fourth vertical level (located at approximately 14 and 100 meters). The stability categories are bound by -0.2 , 0.2 and 0.5 [K/100m], for unstable, neutral, stable and very stable conditions, respectively.

3.4 Wind generalization

Because the winds extracted from a mesoscale model simulation are spatially averaged values representative for the area of the grid box size, they should not be directly compared to those measured *in situ*. In addition, over land, the mesoscale model topography and surface roughness in a grid box and in the surrounding grid boxes are often very different from those around the actual site where measurements were taken, especially in complex terrain. To overcome this problem, a technique of generalization of both mesoscale model output and local measurements has been proposed and used in wind atlas studies (Tammelin et al., 2012; Larsén et al., 2012; Badger et al., 2013). The generalization procedure converts both the measured and modeled winds to a standard condition, over a homogeneous surface with a reference roughness length (e.g., 3 cm) at a reference height (e.g., 100 m).

A comprehensive description of the procedure used to generalize winds derived from the output of mesoscale models is given in Larsén et al. (2012) and Badger et al. (2013). We provide a brief summary here. The speed-up effects due to local orography (e.g. speed-up at hills) and roughness change (e.g. the effects of the internal boundary layer along the coastline) are first calculated and they are represented as the coefficients δA_o and δA_r, respectively. These coefficients are functions of the wind direction sector and height. An effective roughness length is also calculated for each sector, as the area-averaged roughness in the upstream fetch, and denoted as $\hat{z}_0$.

To create a generalized wind climatology, firstly the speed-up effects of orography and roughness change are removed for each sector and each standard height. To generate wind climatologies to be used in WAsP (e.g. via WAsP "lib" files) these heights are normally set to 10, 25, 50, 100 and 200 m. The output from the mesoscale model is interpolated from the model heights, which vary in space and time, to these standard heights. The flat homogeneous terrain wind speed $\hat{u}_z$ at a height of z and uniform roughness $\hat{z}_0$ is obtained through:

$$\hat{u}_z = \frac{u_z}{(1+\delta A_o)(1+\delta A_r)}, \tag{10}$$

where u_z is the observed wind speed at height z. Orography also alters the wind direction, and the change in wind direction is expressed as

$$\hat{\phi} = \phi - \delta\phi_o, \tag{11}$$

where $\delta\phi_o$ is also a function of wind direction sector and height. Once these two equations are used, time series of $\hat{u}_z$ and $\hat{\phi}$ are obtained for the standard heights and a single roughness length $\hat{z}_0$ for each WRF grid square.

The next step of the generalization of the mesoscale winds is to move away from a wind speed that depends on the upstream roughness, $\hat{z}_0$. This is done in three steps. First, the corresponding surface friction velocity, $\hat{u}_*$, is calculated with $\hat{u}_z$ and $\hat{z}_0$, for each sector through the surface logarithmic law:

$$\hat{u}_* = \frac{\kappa \hat{u}_z}{\ln(z/\hat{z}_0)} \tag{12}$$

where $\kappa = 0.4$ is the von Kármán constant. The geostrophic wind, $\hat{G}$, and the angle between the near-surface wind and the geostrophic wind, ϕ_G, are then calculated from $\hat{u}_*$ through the geostrophic drag law for neutral conditions

$$\hat{G} = \frac{\hat{u}_*}{\kappa}\sqrt{\left(\ln\frac{\hat{u}_*}{f\,\hat{z}_0} - A\right)^2 + B^2}, \tag{13}$$

$$\sin\phi_G = -\frac{B\hat{u}_*}{\kappa\hat{G}} \tag{14}$$

where f is the Coriolis parameter, $A = 1.8$ and $B = 4.5$ are dimensionless parameters for neutral conditions. Secondly, the friction velocity $u_*(z_{0j})$ is calculated using the geostrophic drag law interactively for a given set of standard roughness lengths z_{0j}. In a WAsP "lib"

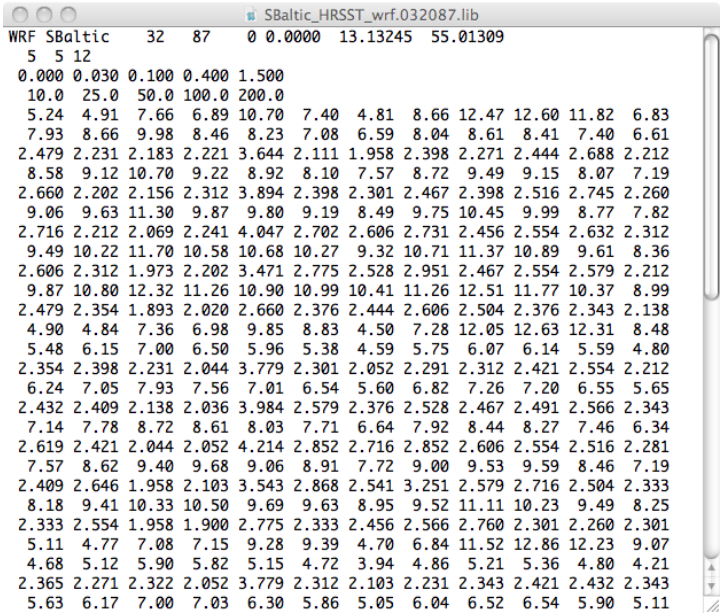

Figure 7: Structure of a WAsP "lib" file.

file, these roughnesses are assigned the values 0.0002, 0.03, 0.1, 0.4, and 1.5 m. Thirdly, the surface logarithmic law is used again to determine $u(z, z_{0j})$ for the standard heights. This is done for each individual hourly wind speed and direction. Therefore, from the original time series of wind speed and direction at each standard level, 25 (i.e., 5 heights and 5 roughness lengths) time series are generated. The 25 time series are then summarized via a Weibull fit for each wind direction sector using the method described in Section 3.2. Figure 7 shows the structure of the resulting WAsP "lib" file.

The WAsP"lib" is structured as Weibull As and ks for each sector, height and standard roughness length. The first row contains information about the geographical location of the wind climate represented in the lib-file. The second row lists the number of roughness classes (5), heights (5), and sectors (12), respectively. In the third and fourth row, the actual roughness (m) and heights (m) are listed. Below these header lines, a succession of frequencies of wind direction (1 line), values of Weibull-A (1 line) and Weibull-k (1 line) for each roughness class and height are printed for each sector (12 sectors per line).

A similar procedure is done for the observed winds from masts and lidars. In this case the generalization is done using WAsP and maps of the real surrounding orography and roughness to the site. Some examples of generalization for both mesoscale winds and observations will be given in section 5. This type of file can be used and displayed (Figure 8) in WAsP.

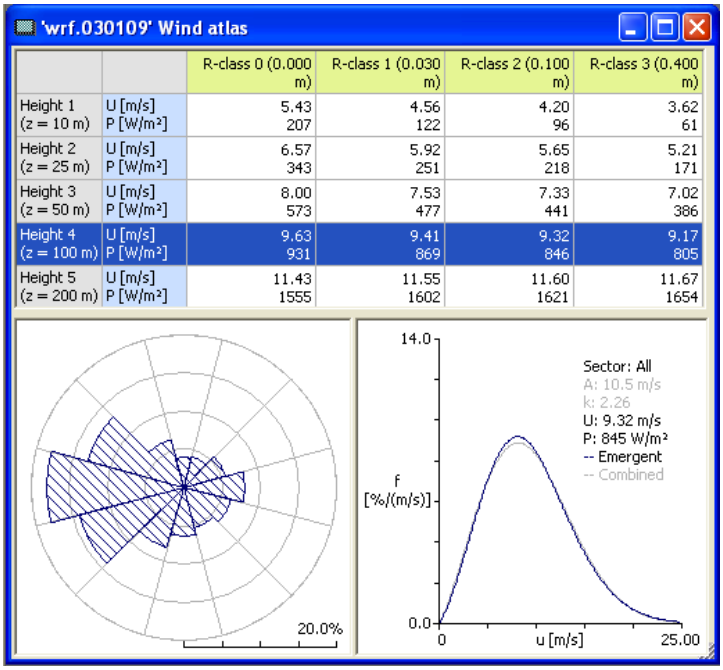

Figure 8: Graphical view of a WAsP "lib" file.

4 Sensitivity Experiments

To run a set of mesoscale simulations to produce a numerical wind atlas the best model configuration needs to be found. This "best" model setup will often depend on the wind climate and the topographic details of region of interest. In addition to finding the optimal model configuration, the sensitivity of the wind climate to details of the model setup provides a first order estimate of the reliability of the wind climate estimated by the mesoscale model.

Several 1-year and longer simulations were conducted to explore the sensitivity of the resulting wind atlas (e.g. annual mean wind speed) and other parameters to details of the model simulations. All the runs are listed in Table 2 below. These experiments concentrate on driving reanalysis, SSTs and a few details of the model parameterizations. An other dimension of sensitivity experiments derives from changing the location, size and grid spacing of the model domains. Sensitivity to the later, though important, is not explored in this report.

Table 2: Details of the various model configurations used in the sensitivity experiments. The "standard setup" is that described in Table 1.

Simulation name	period	driving reanalysis/SSTs	special setup
ERA-HRSST (control)	2006–11	ERA Interim + HRSST	standard setup
ERA	2010	ERA Interim + OISST	standard setup
CFSR	2006–10	CFSR + OISST	standard setup
CFSR-HRSST	2010	CFSR + HRSST	standard setup
ERA-LOWN	2010	ERA Interim + HRSST	reduced nudging const.
ERA-SHORT	2010	ERA Interim + HRSST	daily runs
ERA-YSU	2010	ERA Interim + HRSST	YSU PBL scheme
ERA-YSU2	2006–11	ERA Interim + HRSST	New YSU PBL scheme
ERA-63MYJ	2010	ERA Interim + HRSST	63 vertical levels

4.1 Sensitivity to driving reanalysis

To examine the wind climate sensitivity to the driving reanalysis we repeated the control simulation using the Climate Forecast System Reanalysis (CFSR) from the USA NOAA/NCEP

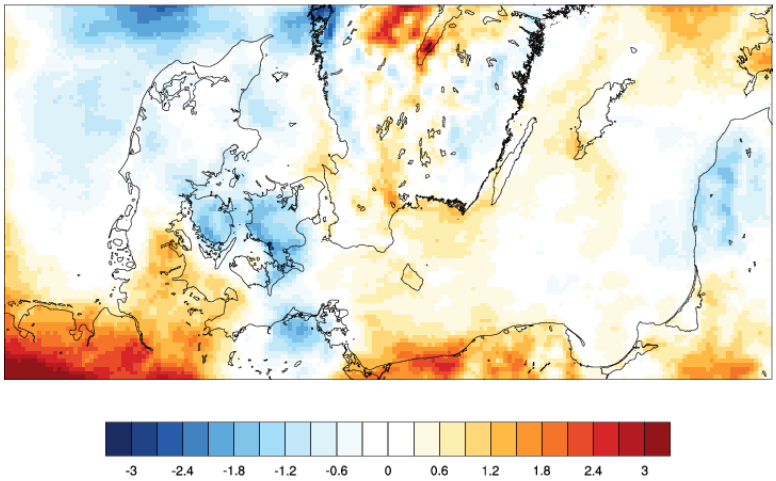

Figure 9: Differences in annual mean wind speed (%) at 100 meters between the ERA-HRSST and CFSR-HRSST simulations (Table 2) during 2010.

(Saha et al., 2010). The extra simulation was carried out during 2006–2010, but for consistency with the other sensitivity simulations, only the results for 2010 are shown here. Figure 9 shows the relative difference in annual mean wind speed between the two simulations. Differences are small in most areas with the largest values of the order of ±3%, which occur mainly near the edges of the smallest domain. This is expected because the information from the reanalysis fields is being nudged into D1 and feed in through the lateral boundaries to D2. Another area with larger negative differences is over the Danish islands of Zealand and Fyn. The reason for such differences is unknown.

4.2 Sensitivity to sea surface temperatures

The sensitivity to the lower boundary conditions used in the simulations was examined by conducting extra simulations where the daily, high-resolution, real-time, global, sea surface temperature (HRSST) available at a horizontal grid spacing of 1/12° is replaced by a coarser product at a horizontal grid spacing resolution of 0.25° (OISST). The SST field from these two sources are interpolated to the WRF model grid and the two maps during the summer months (June–August) are shown in Figure 10. In general, the HRSST provides warmer overall SSTs and stronger gradients near the coast than OISST.

When the annual mean temperatures are compared to each other (not shown), the differences are smaller than those during the summer months. In this region the largest differences

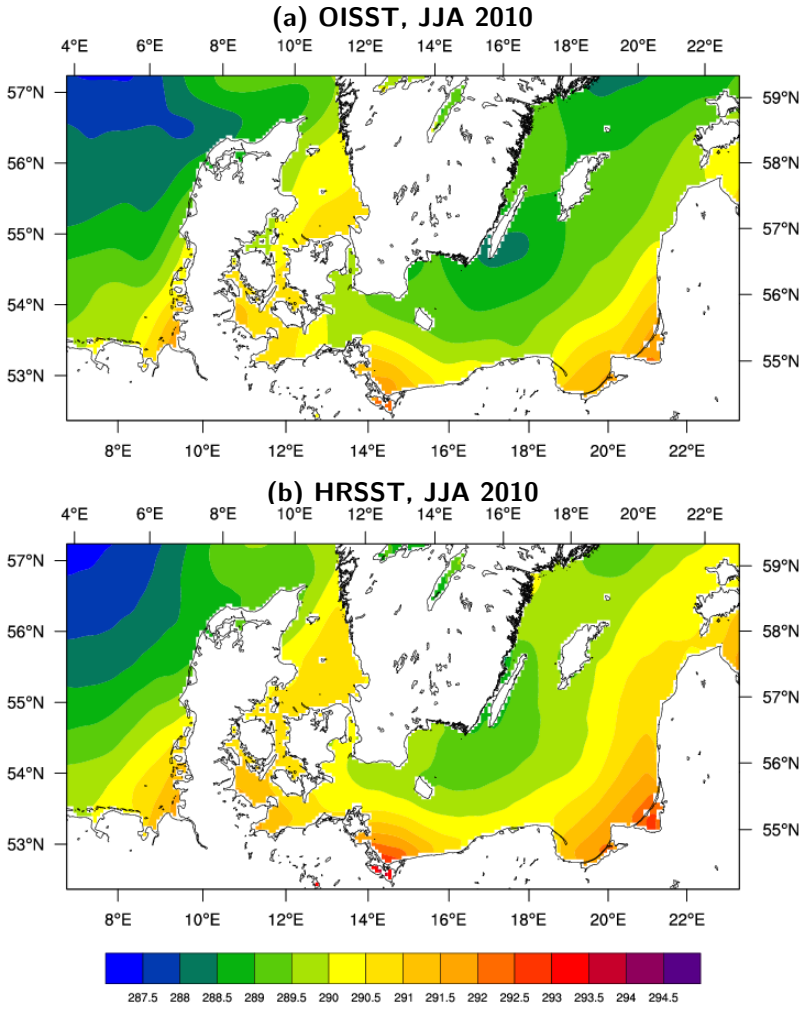

Figure 10: Time averaged sea surface temperatures (SST) during June–August 2010 in the (a) OISST and (b) HRSST datasets interpolated to the WRF model domain.

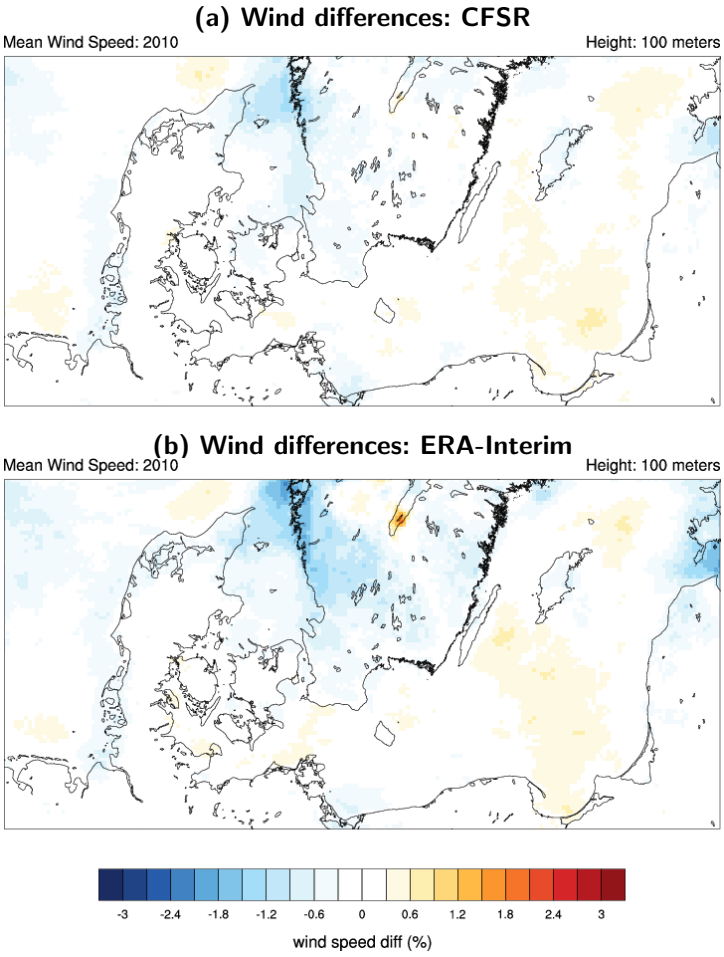

Figure 11: Differences in annual mean wind speed (%) at 100 m between: (a) CFSR and CFSR-HRSST simulations and (b) ERA and ERA-HRSST simulations.

in SST (not shown) are seen along the west coast of Denmark and Sweden, with warmer (up to 2°C in the annual mean) SSTs in the HRSST dataset. These are the same areas where the annual mean winds show the largest differences in the two panels of Figure 11. Annual mean wind speeds are larger (negative areas) in the climatology generated from annually averaged warmer SSTs. However, these differences are smaller (1–2%) compared to those seen in the climatologies generated from the two different reanalysis. But, it is interesting to see that the response to the differences in SST depends on the reanalysis used: the differences in wind speed are larger when the ERA-Interim is used instead of the CFSR reanalysis. In addition, it is expected that in areas where the wind regime is driven by thermal contrast (for example areas dominated by sea breeze during the summer months and further south in Europe) the sensitivity could be stronger.

4.3 Sensitivity to nudging and re-initialization frequency

In the method used here to run long-term simulations with WRF, the model is run with extra nudging terms for horizontal winds, temperature and water vapor. These terms warranty that the model large scale dynamics does not deviate much from that given in the large-scale reanalysis fields. Some of the advantages of the use of nudging are outlined in Miguez-Macho et al. (2004). In the control simulation (Table 1), nudging is done on the outer domain only and above level 10. The nudging coefficient, which is a measure of the nudging strength, is set to 0.0003 s^{-1} (equivalent to a relaxation time scale of about an hour).

To study the impact of this parameter on the wind atlas fields, we conducted an additional

run where the nudging constant was reduced to 0.000075 s^{-1} (equivalent to a relaxation time of about 4 hours). This is simulation ERA-LOW in Table 2. In Domain 1 (not shown), some small differences ($\sim$1%) exist between the two simulations. The differences in annual mean wind speed (not shown) in these two simulations are negligible (max absolute differences $<$1%).

Another way of studying the effect of nudging on the simulations is to disable this option.

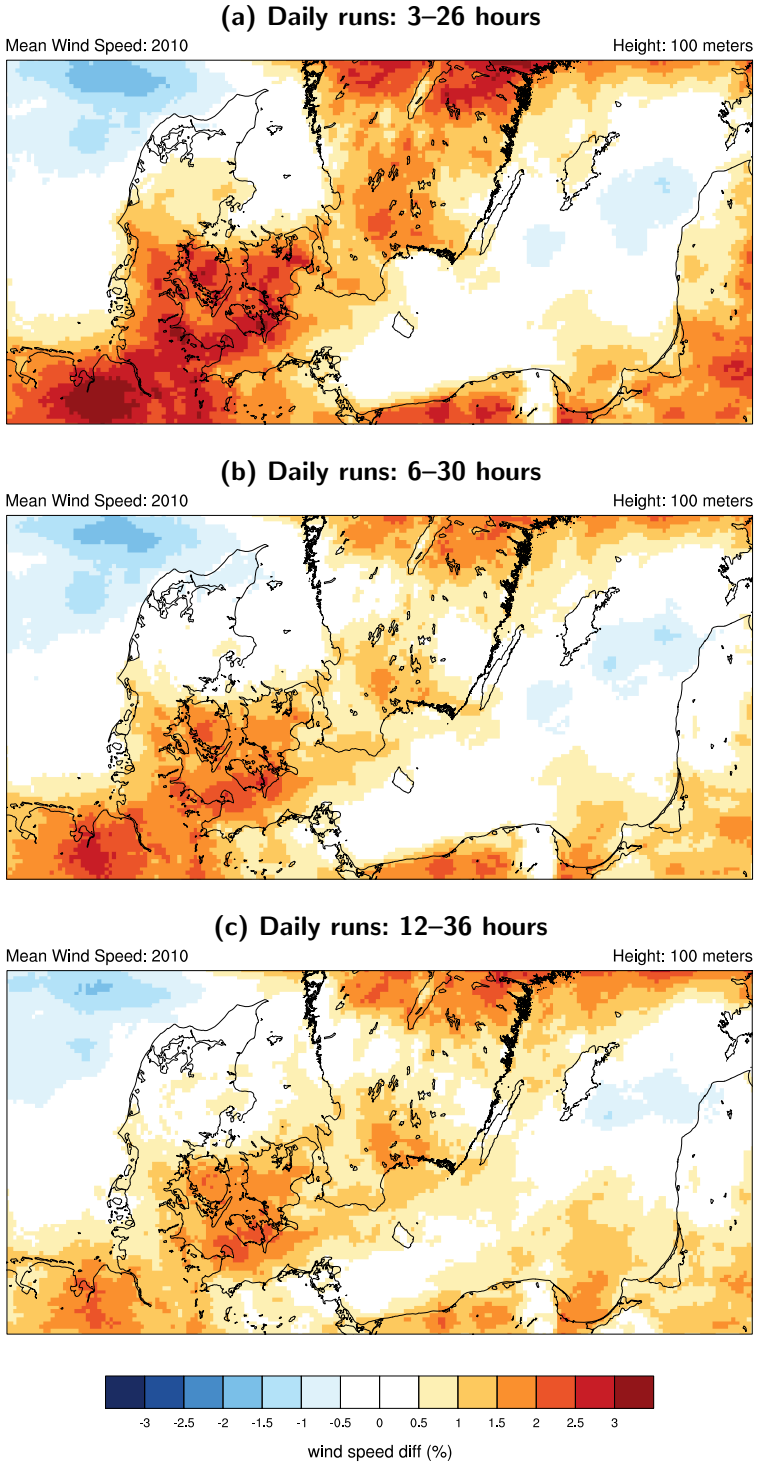

Figure 12: Differences in annual mean wind speed (%) during 2010 at 100 m between the ERA-HRSST simulation and that produced from short daily runs (ERA-SHORT) for different averaging periods: (a) 3–26, (b) 6–30, and (c) 12–36 hours.

A second year-long simulation was conducted using short runs (each 36 hours long) that are re-initialized daily instead of every 10 days in the control and all other simulations shown here. The daily simulation method is used by many wind energy companies that provide mesoscale model output (Vortex, personal communication) and it was used in the North Sea and Irish Sea wind atlases in NORSEWInD.

The differences in annual mean wind speed during 2010 between the control simulation and the mean wind speed derived from the output of the short simulations is presented in Figure 12. The 3 plots show that the length of time that is discarded as spin-up in the simulations (i.e. 3, 6, or 12 hours) can affect the mean wind speed estimate. Differences are up to 3% over most land areas in the mean constructed from the 3–26 hours forecasts (Figure 12a) than in the long simulations. That is, the mean wind speeds are larger in the control than in the climatology constructed from the short daily runs. However, the differences decrease as the spin-up period is increased. We hypothesize that this is due to the spin-up time required to reach a balance between the evolving initial conditions and the model physical parameterizations. Part is due to the re-initialization of land surface conditions (e.g. soil moisture) and its impact on surface-layer stability and the wind profile, but further investigation is necessary. It is more obvious that over oceanic areas differences are small because spin-up effects are not as important as they are over land.

4.4 Sensitivity to number of vertical levels

To study the sensitivity of the mean annual wind speed and other wind-energy relevant parameters to the number and position of vertical levels simulations ERA-HRSST and ERA-63MYJ are compared. In ERA-HRSST there are 6 levels located under 200 m from the surface approximately at 14, 43, 72, 100, 129 and 190 m. In ERA-63MYJ, 14 levels are located below 200 m at approximately 14, 33, 43, 52, 62, 72, 81, 90, 100, 111, 123, 139, 158, 180 m.

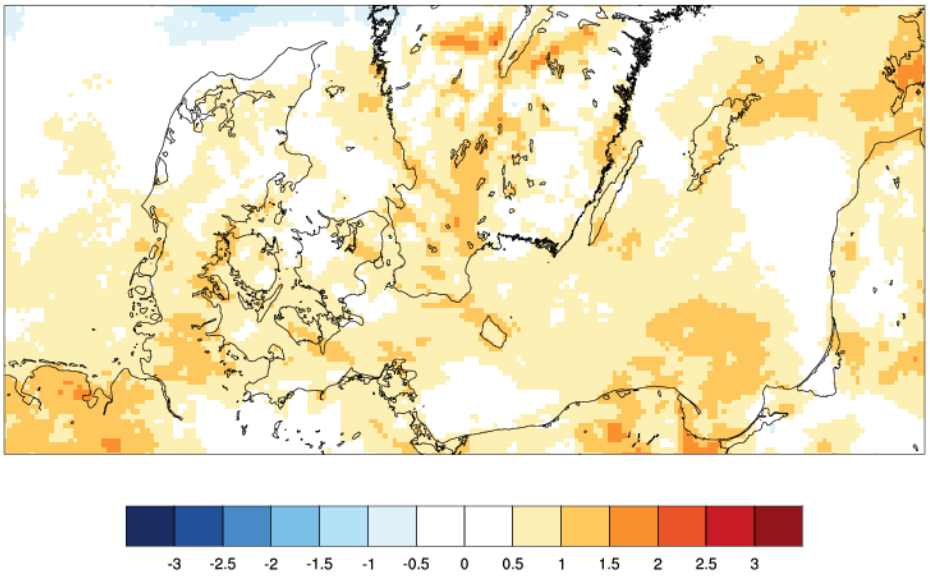

Figure 13: Differences in annual mean wind speed (%) at 100 meters between the ERA-HRSST and ERA-63MYJ simulations (Table 2) during 2010.

The differences in mean annual wind speed between these two simulation at 100 m are shown in Figure 13. Overall differences are small ($< 1.5\%$) and positive, meaning that a increased number of vertical levels results in lower mean annual wind speed at 100 m. No particular spatial pattern can be established.

Even though differences in annual mean wind speed are small, other parameters related to the wind shear might change by the addition of vertical levels in the model PBL. We

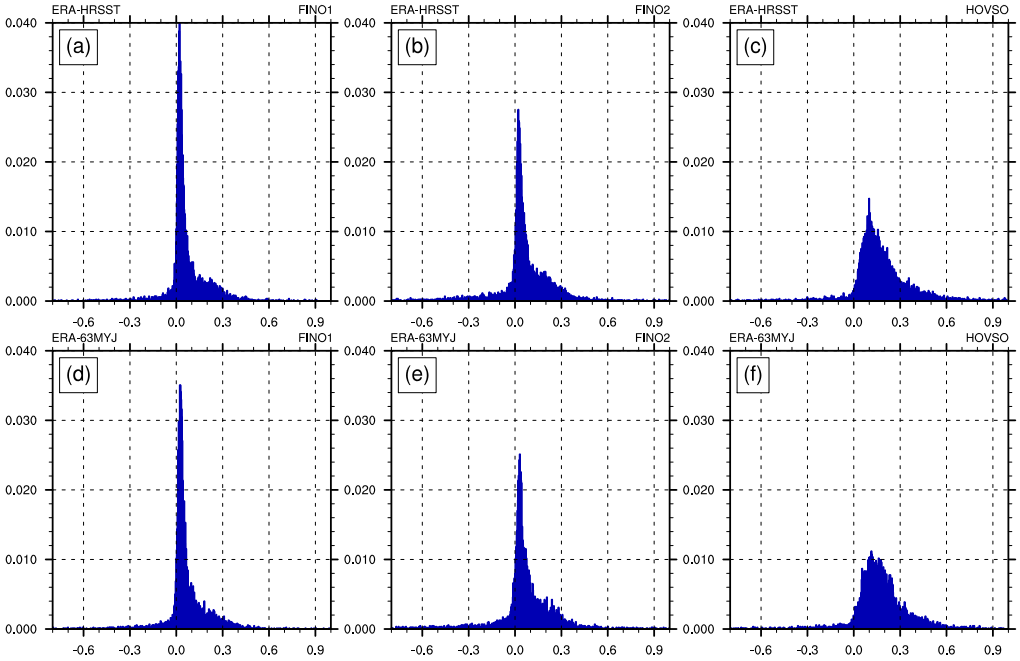

Figure 14: Frequency distributions of the value of α for the two model simulations: ERA-HRSST (top row) and ERA-63MYJ (bottom row) during 2010 at the model grid point closest to: FINO1 (a) and (d), FINO2 (b) and (e), and Høvsøre (c) and (f).

have computed the mean annual wind shear parameter from the wind speed time series from these two runs. We used the method described in Section 3, so that the calculation of α is independent of the location and number of vertical levels. The maps of the time-mean of α (not shown) are almost identical to each other over water.

To investigate this issue further, Figure 14 shows the frequency distributions of α for three model grid points close to measurement sites: FINO1, FINO2 and Høvsøre. Their location is shown in Figure 17. The figure shows that there is a general tendency for narrower distributions with fewer vertical levels compared to the simulation with high vertical resolution (ERA-63MYJ), but the differences are very small. This tendency can be explained by the fact that an increased number of levels could allow for a larger range of α to be simulated.

4.5 Sensitivity to PBL scheme

We also conducted a series of yearlong simulations to identify the sensitivity of the simulated wind climate to the PBL scheme used. While many different PBL schemes (over 10 in WRF version v3.4) are available to run with WRF, we concentrate on the two most used schemes: the Mellor-Yamada-Janic, MYJ for short (Mellor and Yamada, 1982) and Yonsei University, YSU for short (Hong et al., 2006). The YSU scheme has undergone several changes in the versions coupled in WRF. We call YSU2 (Table 2) to the version implemented in WRF v3.4.1 and released on August 16, 2012. In our simulations we still run WRF version 3.2.1 but the new YSU scheme replaces the old version of the YSU scheme. So the only difference between the YSU and YSU2 experiments is in the PBL scheme itself and the way it is coupled to the land surface model. The YSU2 scheme fixes a bug that made the eddy diffusivity too large under stable conditions.

The effects of the introduction of the new scheme are clear and consistent throughout the model domain. Figure 15a shows the differences in annual mean wind speed at 100 m between simulations with the old YSU (simulation ERA-YSU) and the new YSU PBL (simulation ERA-YSU2). Differences are positive throughout the domain, i.e. stronger winds in the simulation using the old scheme, with maximum of about 0.6 m s^{-1} over eastern Sweden. This pattern is

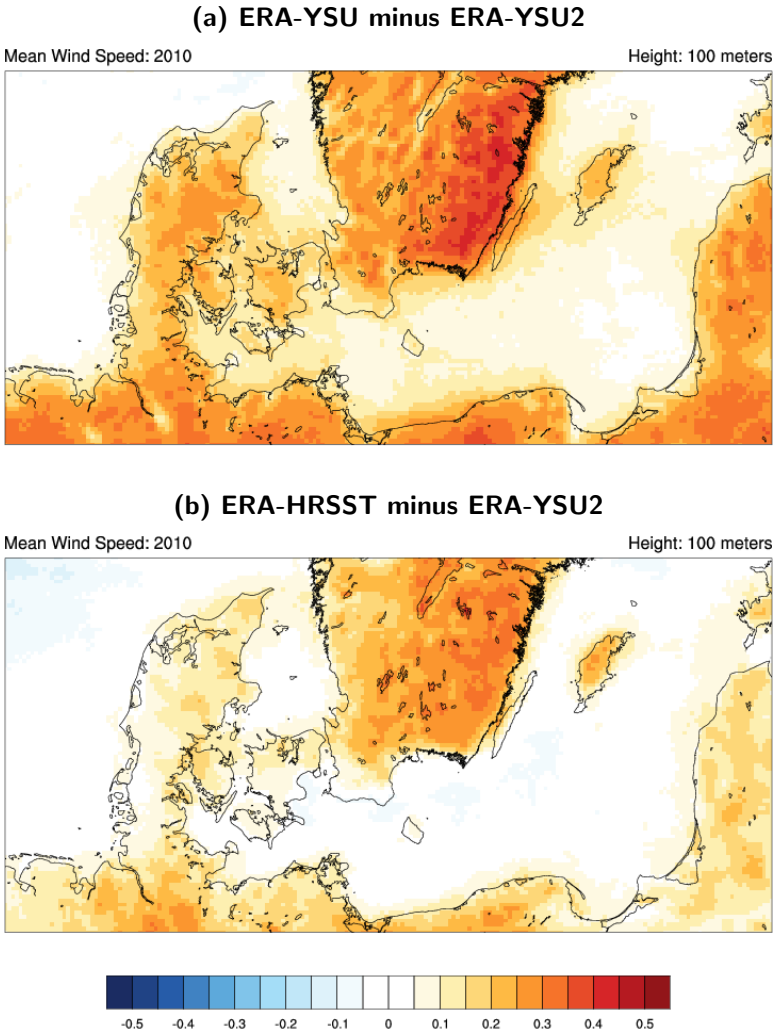

Figure 15: Difference in mean annual wind speed ($\mathrm{m\,s^{-1}}$) at 100 meters: (a) ERA-YSU minus ERA-YSU2 experiments, and (b) ERA-HRSST minus ERA-YSU2 experiments.

related to the prevalence of stable conditions over land in this area. The influence extends into the adjacent water downstream from the coasts (see Figures 35 and 36). These differences are far larger (up to 6%) than those in any of the other sensitivity experiments in Table 2. The differences between the control run (ERA-HRSST) and that conducted with the new YSU scheme are also large (Figure 15b) but confined to the land area.

In Figure 16 we show the frequency distribution of the shear parameter, α, for three sites and the three WRF simulations: ERA-HRSST, ERA-YSU, and ERA-YSU2. This demonstrates that even though the mean wind speed might be insensitive to the choice of PBL scheme other model parameters can be impacted. While the distributions for the ERA-HRSST (MYJ PBL scheme) and ERA-YSU2 are quite similar and resemble those of the observations in Peña et al. (2012), those for the ERA-YSU are quite different. This is particularly marked at Høvsøre in Figures 16 (c), (f) and (i). It is also interesting to note that the secondary peak in the ERA-YSU α distributions at all sites is apparently due to the wrong formulation. It will be quite interesting to investigate these differences in more detail in a follow up study.

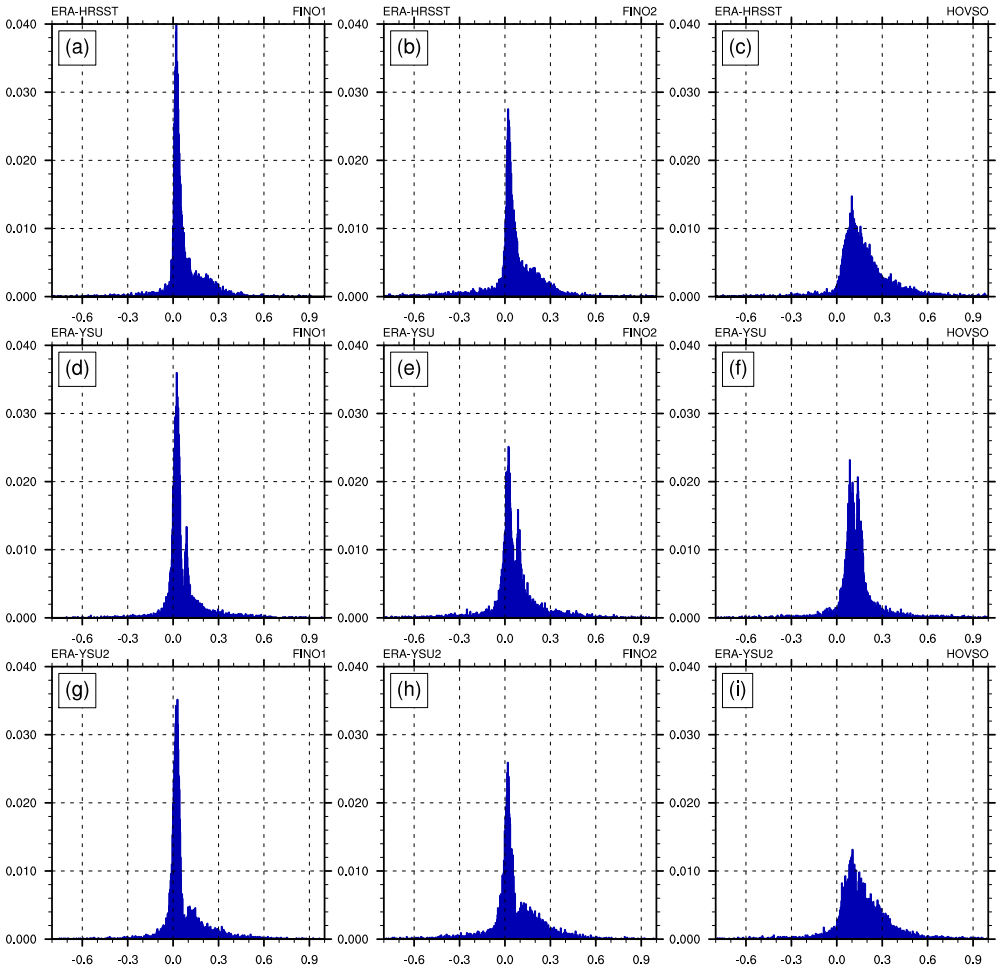

Figure 16: Frequency distributions of the value of α for the three model simulations: ERA-HRSST (top row), ERA-YSU (middle row), and ERA-YSU2 (bottom row) during 2010 at the model grid point closest to: FINO1 (a), (d) and (g), FINO2 (b), (e) and (h), and Høvsøre (c), (f) and (i).

5 Verification

5.1 Mean wind speeds

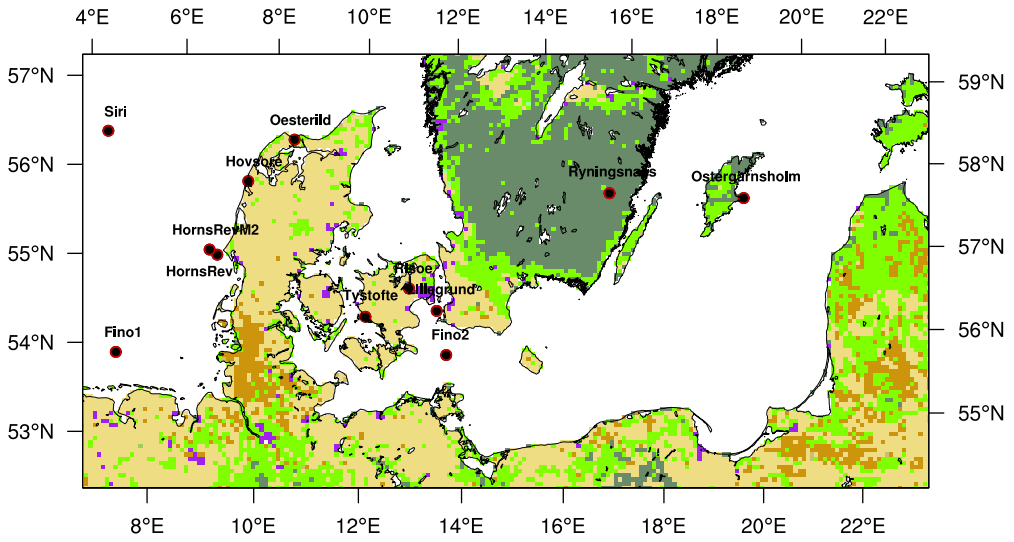

Figure 17: Location of the verification stations in the North and Baltic seas.

The time-average wind speeds simulated by WRF are compared against observations in Table 3 for several sites in the North and Baltic Seas. The verification sites are presented in Figure 17. Most validation sites are tall mast, but two, Siri and Horns Rev II are lidar sites.

To compute the values in Table 3 hourly model-simulated wind fields are interpolated to the observation height and geographical location of the site (using separate zonal and meridional winds from the WRF output) and they are paired in time. This guarantees that the same number of samples is used in the observations and the model results. The highest level or that closest to a height of 100 m is chosen for the verification and it is listed in Table 3. We disregarded any wind speed observations with wind speed lower than 0.3 $\mathrm{m\,s^{-1}}$.

The first 8 sites in Table 3 are offshore and their mean absolute error is 2.9%. The largest error is at Lillgrund (8.2%), but the measurements at this site are relatively low (65 m) and are influenced by a wind farm immediately to the northeast of the mast. In addition, measurements are only available for one year (2009) and the location near the Swedish coast and in the relatively narrow channel between Denmark and Sweden make this site quite challenging for the coarse resolution of the mesoscale model. In all other sites the mean absolute error is lower than 3.9%. At FINO1 the error is smaller than 1% at 90 meters. There is no consistent sign of the wind speed bias at the sites: the winds are overestimated at FINO1, Lillgrund, Östergarnsholm, Horns Rev M2 and Siri, and underestimated at FINO2, Horns Rev and at the commercial site near Öland.

Over land the errors are much larger than offshore as expected. On average, the mean absolute error for these 5 sites is 8%, with WRF overestimating the observed wind speeds at most sites. Errors at the coastal site of Høvsøre are comparable to those offshore (1.2%). Errors at Ryningsnäs are particularly large (21%). This site is located over eastern Sweden surrounded by 20–25 m tall managed spruce coniferous forest and two wind turbines with hub heights at 80 and 100 m and 90 m rotor diameters. The land surface scheme in WRF does not take into account the displacement height of the vegetation. If we consider a displacement height of 20 m when extracting winds from the simulation, the relative error is reduced to 13% (Table 3).

We examine now in detail the winds simulated and observed at all offshore sites and at

Table 3: Comparison of observed and WRF-simulated mean wind speeds across the domain in the ERA-HRSST simulation. The first 8 sites are offshore, the last 6 on land. Siri and Horns Rev II are lidar sites. NOBS is the number of hourly observations used. *The second estimate of annual mean wind speed for Ryningsnäs used a displacement height of 20 m for the WRF-derived winds.

Met mast	time period	NOBS	height (m)	U OBS ($m\,s^{-1}$)	U WRF ($m\,s^{-1}$)	Error (%)
FINO1	04.01.2006–14.04.2011	49516	90	9.38	9.47	1.0
FINO2	01.08.2007–31.12.2011	31927	90	9.46	9.30	-1.7
Horns Rev (M7)	25.12.2005–15.12.2009	29401	70	9.52	9.49	-0.3
Lillgrund	08.01.2009–31.12.2009	8615	65	7.56	8.18	8.2
Östergarnsholm	22.01.2007–20.10.2009	16151	16	6.41	6.75	3.9
CS (Öland)	08.06.2006–08.06.2009	26642	50	7.83	7.32	-6.5
Siri	02.06.2010–24.07.2011	3461	105	10.51	10.17	-3.2
Horns Rev II	25.06.2009–19.08.2011	15543	106	9.48	9.82	3.6
Høvsøre	04.01.2006–31.12.2011	50998	100	9.24	9.12	-1.3
Østerild syd	15.04.2010–14.04.2011	12046	44	5.69	6.44	13.2
Østerild vest	03.05.2010–02.05.2011	8411	44	6.12	6.66	8.8
Risø	04.01.2006–31.12.2006	8702	76	6.58	6.67	1.4
Risø	04.01.2006–31.12.2006	6500	125	7.07	7.24	2.4
Ryningsnäs	18.11.2010–31.12.2011	9323	98	5.86	7.10	21.2
Ryningsnäs*	18.11.2010–31.12.2011	9323	98*	5.85	6.61	13.0

Høvsøre. The advantages of generalization for a number of land sites will be explored in Section 5.4.

5.2 Wind speed distributions and profiles

We show here graphical representations of the observed and model simulated wind climatologies for all available offshore sites within the model domain. For these sites we show: wind speed distribution and wind roses for the level closest to 100 m and mean wind speed profile for all available levels. In the distributions and wind roses the observation and model winds are collocated. In the mean wind profiles the same number of samples are used in all levels.

FINO1

The graphical verification of the WRF model winds against observations are presented in Figure 18 for the FINO1 site. Since the analysis of the observations in Peña et al. (2012) revealed unrealistic wind rose at 100 m, we choose to use the observations at 90 m for the verification presented here.

The mean error in mean wind speed at 90 m at this site is 1.0%. The biases are positive at all levels (i.e., winds are overestimated in the model simulations) and are quite uniformly distributed with height. The wind roses show very good correspondence but there seems to be a small angle difference between the model winds and the observations: observations are more southerly than the winds from the WRF simulation. There is also a slight shift in the peak of the distribution between the observations (peak at 8–9 m s^{-1}) and the model simulated winds (peak at 9–10 m s^{-1}). This tendency is also visible in the wind roses with slightly more weak winds in the simulations than in the observations, specially in the northwest sector. However, the low winds from the northwest sector (315°) in the observations appear unrealistic and might be a consequence of flow distortion due to the mast and boom (Peña et al., 2012). In addition, in a wind farm was Alpha Ventus wind turbines east of the Fino 1 platform as they were erected in 2009 and the measurements here analyzed are until 2007.

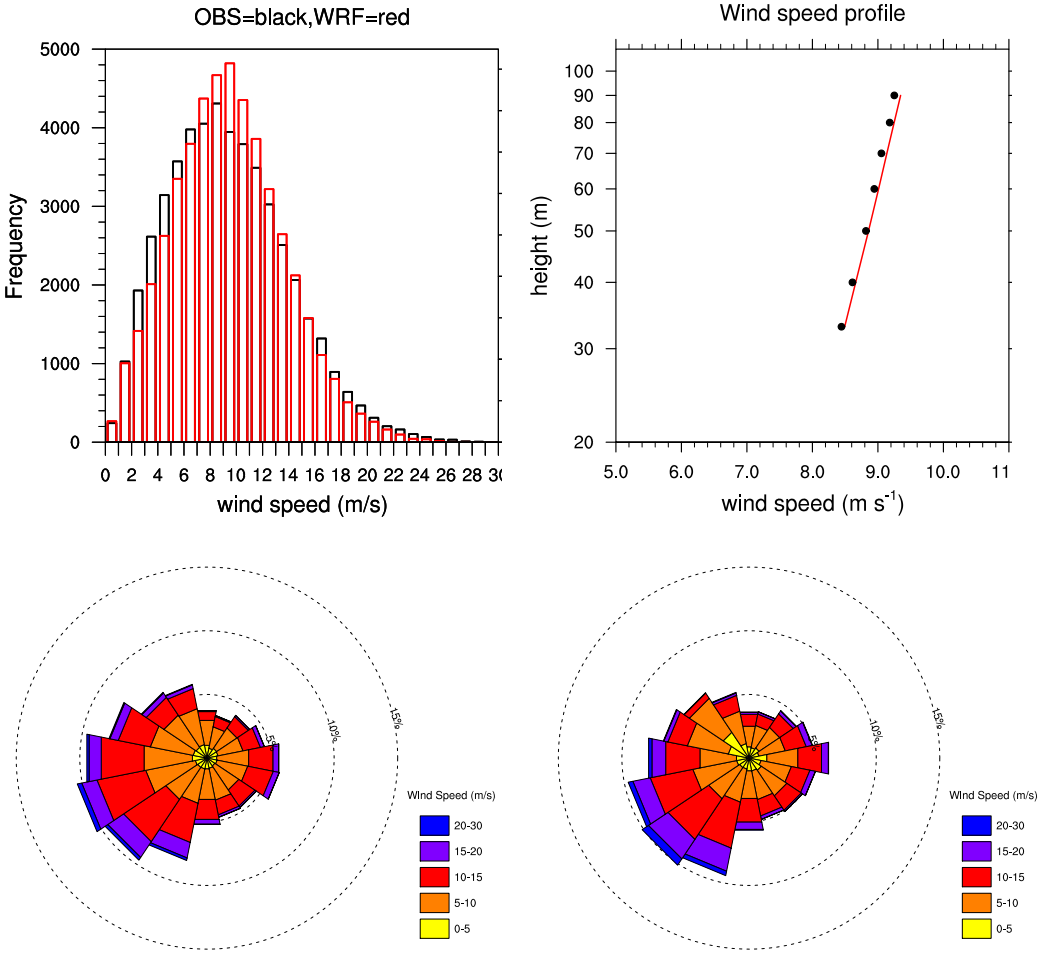

Figure 18: Wind speed distribution at 90 m (top left; OBS=black lines, WRF=red lines), mean wind speed profile (top right; OBS=black dots, WRF=red line) and wind roses at 90 m for FINO1 (WRF=bottom left, OBS=bottom right).

FINO2

Verification plots for FINO2 are shown in Figure 19. As with FINO1, we do not use the values observed at 102 m AMSL because an a priori analysis revealed an unrealistic range of wind shears when using the highest level.

The error in mean wind speed at 92 m at this site is −1.7%, and as with FINO1, the biases are quite uniformly distributed with height. However, at this site the WRF-simulated winds underestimate the observations at all levels. This underestimation might be due to the decrease in winds due to coastal effects in the WRF simulations. Because of the relatively low resolution of the WRF simulations, the simulated fetch is longer than it is probably expected in this region. The wind speed distribution, as at FINO1, shows that the simulated wind distribution is slightly narrower than that from the observations. The wind roses are quite similar both in angle distribution and in wind speed for each sector; although the observed winds are slightly more westerly than those derived from the WRF simulations.

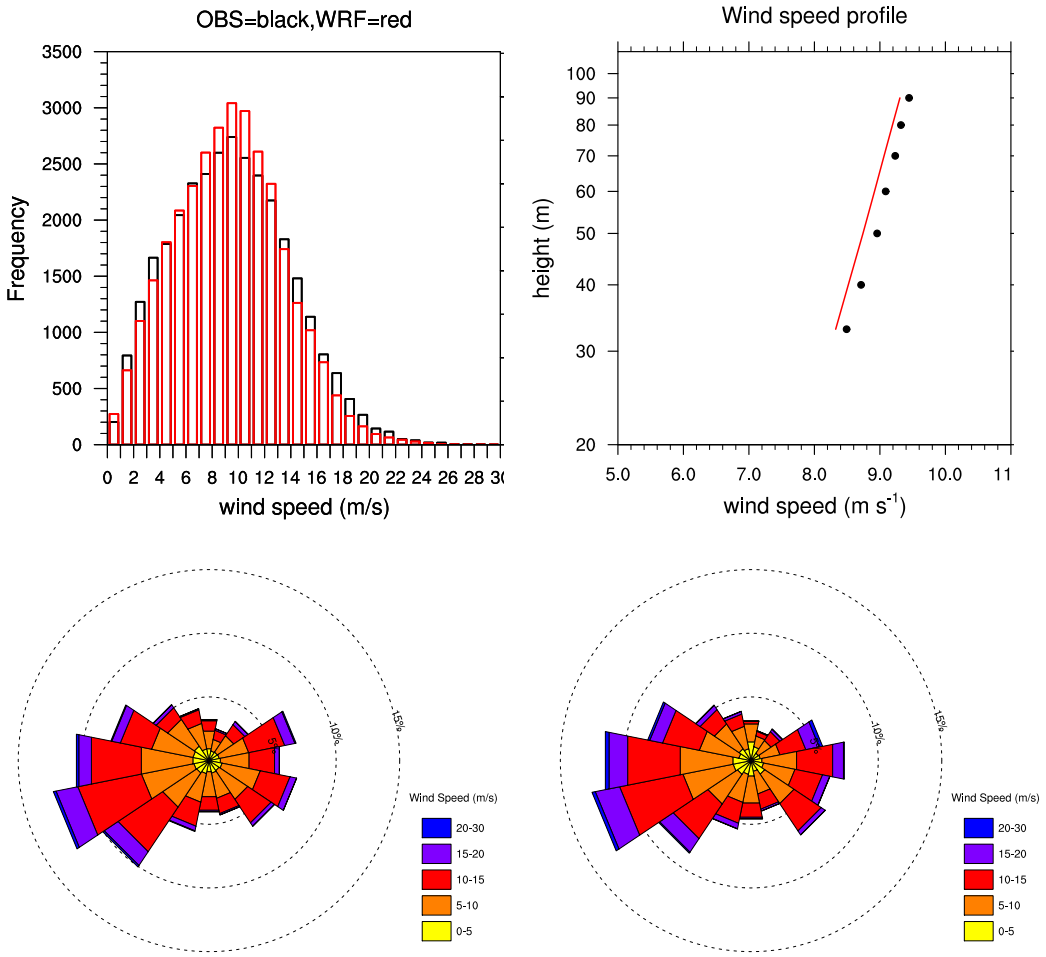

Figure 19: Wind speed distribution at 92 m (top left; OBS=black lines, WRF=red lines, mean wind speed profile (top right; OBS=black dots, WRF=red line) and wind roses at 92 m for FINO2 (WRF=bottom left, OBS=bottom right).

Horns Rev (M7)

The plots for Horns Rev (M7) are presented in Figure 20. As with FINO1 and FINO2 there is excellent correspondence between observed and WRF-derived winds. The mean error in mean wind speed at 70 m is −0.8% at this site. The simulated mean wind speed profile shows positive bias in 20–60 m and a negative bias above at 70 m. The wind speed distributions from observations and the model simulation are also very similar. There is also good correspondence in the directional distributions shown in the wind roses. The lowest frequency of direct westerlies in the observations is very well captured by the WRF-derived winds. However, the 70 m wind speed measurement (performed by a cup anemometer on a pole) systematically shows a higher wind speed compared to the extrapolated 70 m value using the lower measurement levels (Peña et al., 2009).

The winds at M7 mainly come from the west sectors with almost no wind coming from the north-east sector (Figure 20). Therefore, most of the wind measurements are affected by the wake of the Horns Rev I wind farm and thus the observed winds at and below 60 m are underestimated.

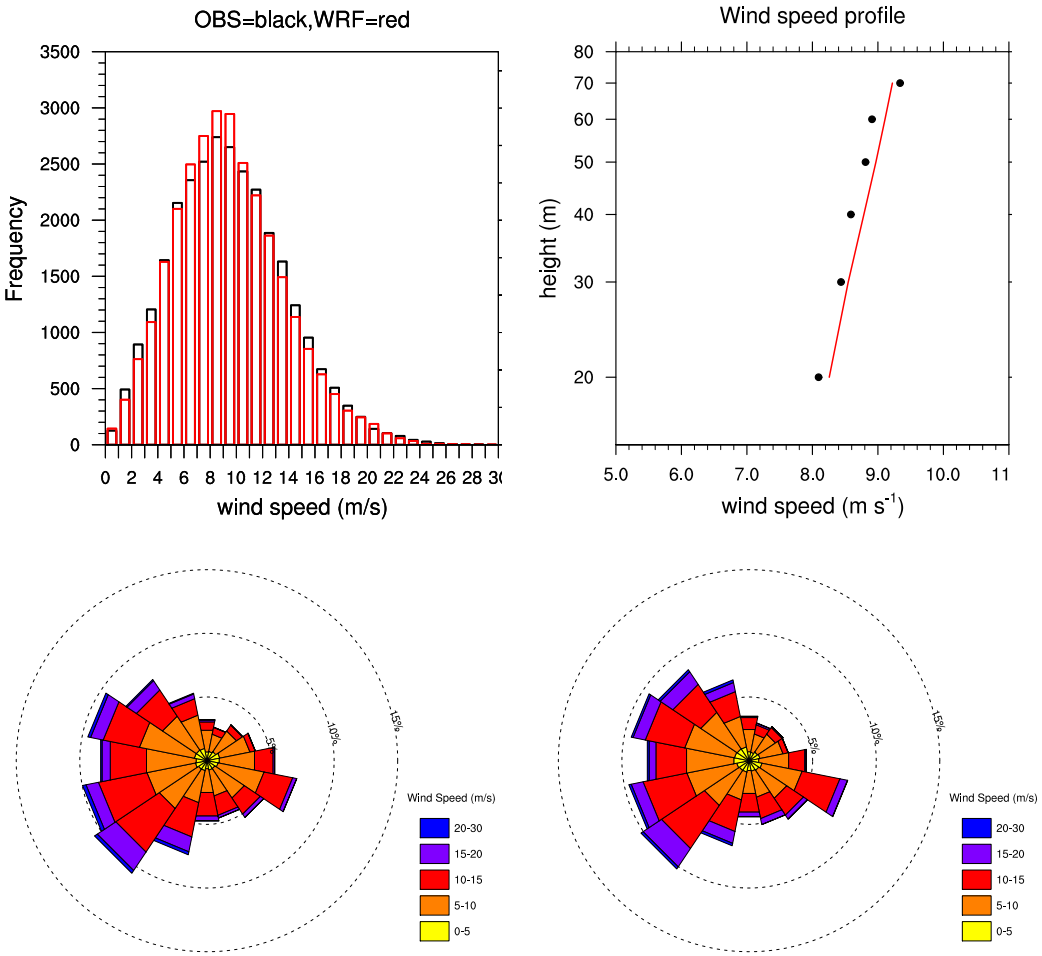

Figure 20: Wind speed distribution at 70 m (top left; OBS=black lines, WRF=red lines), mean wind speed profile (top right; OBS=black dots, WRF=red line) and wind roses at 70 m for Horns Rev M7 (WRF=bottom left, OBS=bottom right).

Lillgrund

Comparison of the observed and WRF-derived wind climatologies for Lillgrund are shown in Figure 21. The height of the anemometers (at 65 m) is lower and the verification period is much shorter than for the previous sites. Thus, the agreement is much poorer than at FINO1, FINO2 and HR M7. The WRF-derived winds are much stronger than those observed at the site. This is apparent in both the wind speed distributions and mean wind profile. The met mast at Lillgrund is located south west of the Lillgrund wind farm and thus winds from the directions 345–100° will be affected by the wake of the wind farm. This effect is easily seen in the wind roses made from the WRF output as compared to the observations. In addition, the observed wind rose does not show any northerly winds. We do not have information related to the placement of the wind vanes at the met mast at Lillgrund but such a lack of winds might be an artifact of the measurements.

Verification of the WRF-derived winds at this site is complicated by the fact that the WRF grid point used is close to land and that the measurements are contaminated by the presence of the wind farm and other measurement artifacts. In addition, few measurements (<9000) have been used in the validation.

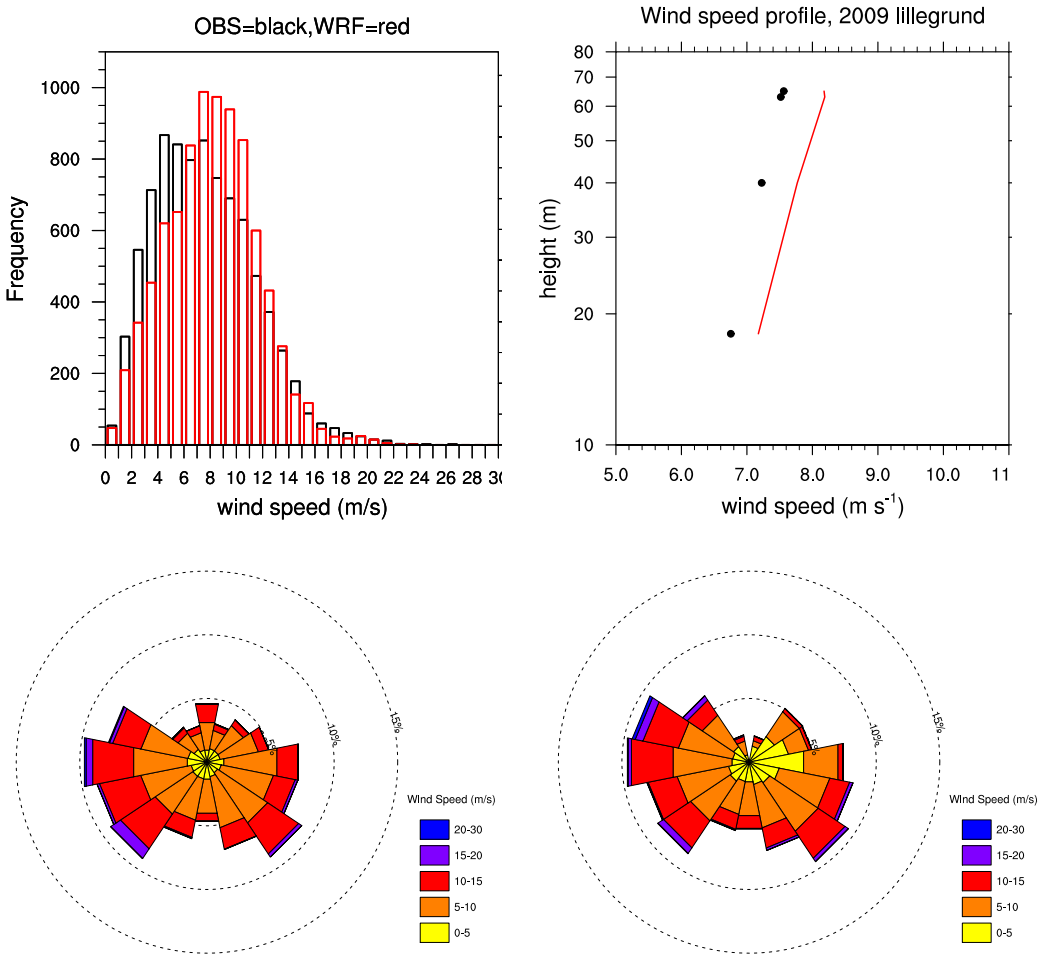

Figure 21: Wind speed distribution at 65 m (top left; OBS=black lines, WRF=red lines), mean wind speed profile (top right; OBS=black dots, WRF=red line) and wind roses at 65 m for Lillgrund (WRF=bottom left, OBS=bottom right).

Östergarnsholm

Wind climatologies from observed and simulated winds at Östergarnsholm are shown in Figure 22. This site is owned and maintained by Uppsala University. The site is located at the southernmost tip of an island east of the island of Gotland, Sweden. The wind rose at this site shows very well the mast relationship to land, with dominant wind directions from the southwest and northeast. Locally, however, the measurements are not very much influenced by the presence of land, specially in view of the predominant wind direction from the southwest.

The winds derived from the WRF simulation overestimate the wind speed at this site, but the measurement heights are low and thus expected to be higher errors than at sites with higher measurement levels. Biases in mean wind speed are smaller at 16 than at 30 m though. The overall directional distribution is well captured by the WRF-simulated winds, but wind roses show a much narrow wind directions from the south-west in the observations than in the model simulations. This is partly due to the details of the topography of the site which are not represented well in the WRF simulations.

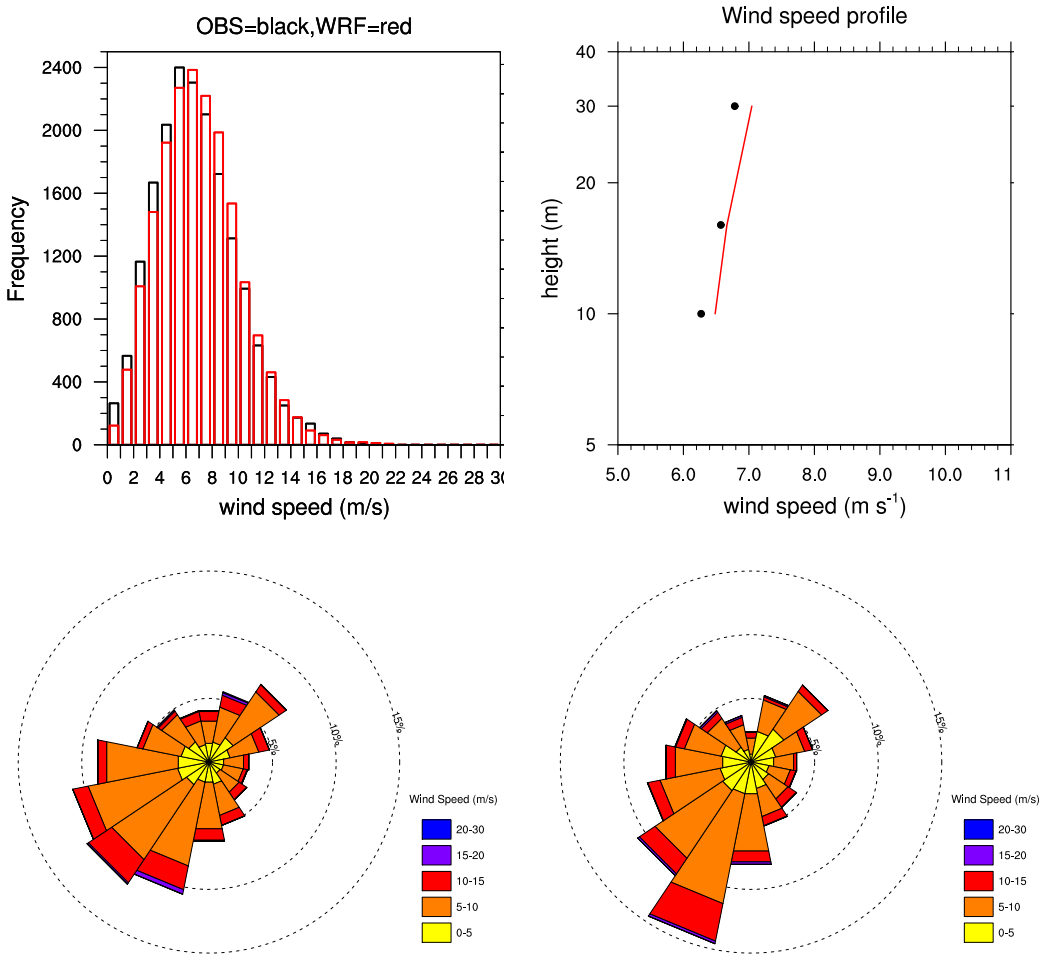

Figure 22: Wind speed distribution at 30 m (top left; OBS=black lines, WRF=red lines), mean wind speed profile (top right; OBS=black dots, WRF=red line) and wind roses at 30 m for Östergarnsholm (WRF=bottom left, OBS=bottom right).

Commercial Site (Coastal Öland)

This site is located in the coastal zone east of the Swedish island of Öland. The comparison of observed and WRF-simulated winds is carried out in Figure 23. The winds derived from the model simulation underestimate the observed winds at all heights, and the bias gets larger with height, -0.28 m s^{-1} at 10 m to -0.51 m s^{-1} at 50 m. At 50 m the wind speed relative error is -6.5%. This is a difficult site for the WRF model to simulate well since the topography and roughness are complex and the mast is located very close to land. Therefore, it is located in the WRF "land shadow" and influenced by the local topography. In addition, the reliability of the measurements is also in question given the unrealistic total absence of northerly winds seen in the wind rose derived from the observations.

Overall the directional wind distribution is well captured by the WRF-derived wind climatology, with a slight more westerly component in the WRF-derived winds. This site will be ideal for investigating the added value of the generalization of the winds simulated by WRF. But, because of confidentiality issues, this cannot be carried out.

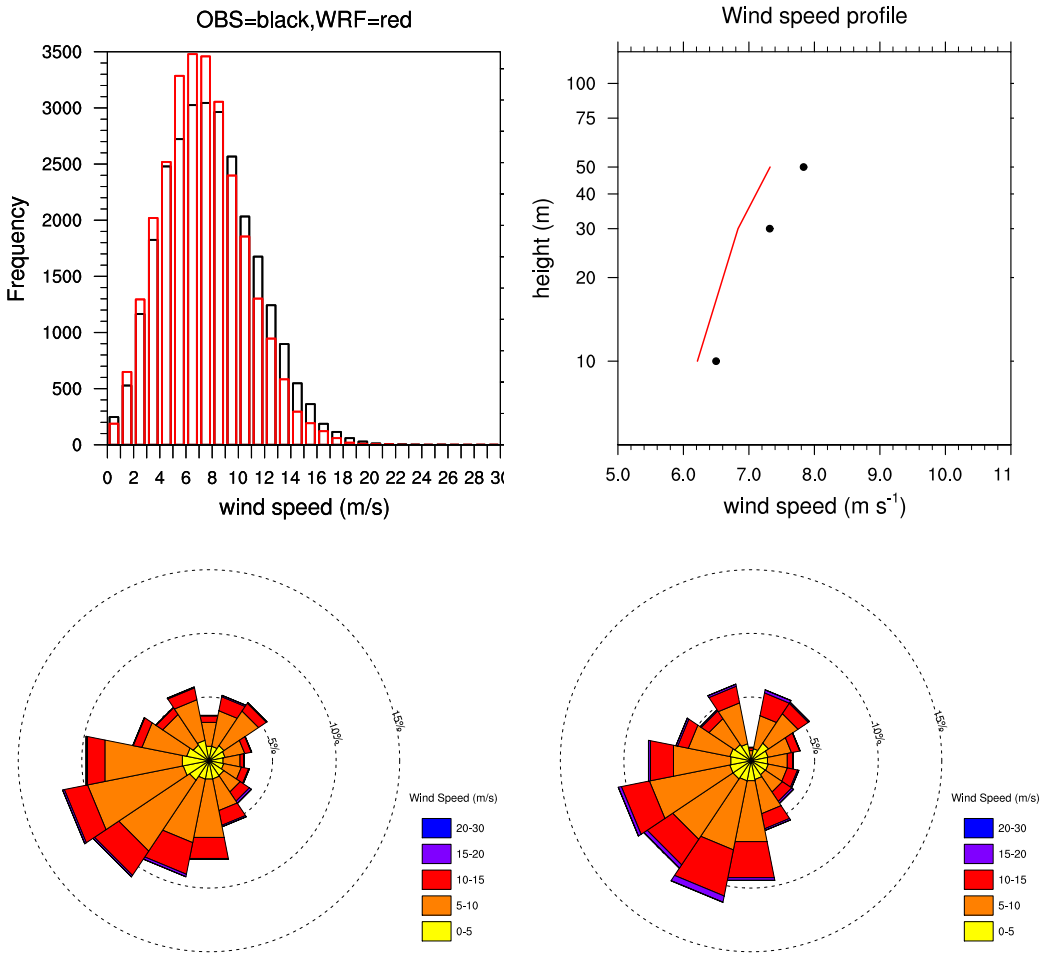

Figure 23: Wind speed distribution at 50 m (top left; OBS=black lines, WRF=red lines), mean wind speed profile (top right; OBS=black dots, WRF=red line) and wind roses for a commercial site in the Baltic Sea near Öland at 50 m (WRF=bottom left, OBS=bottom right).

Siri

This wind lidar was placed on the Siri oil platform and is the sensor installed the furthest offshore in the NORSEWInD project. The winds at Siri mainly come from the northwest sector and almost no wind coming from the northeast sector is observed (Figure 24). However, this wind rose should be interpreted carefully since the amount of available measurements for the months November–May (mainly the winter months) is very low compared to the summer months (Peña et al., 2012). In addition, the wind speeds at lower levels can be influenced by the platform's flow distortion.

The comparison between observations and model winds is still fair, and it shows that the peak of the wind speed distribution is shifted towards lower values in the WRF-simulated winds compared to the observations. The relative error in wind speed at 105 m is −3.2%. Part of the explanation of this underestimation is apparent in the wind roses: the strongest winds from the northwest are not properly represented in the WRF wind climatology. Figure 17 shows that this site is located quite close to the model western edge and this fact could explain the underrepresentation of the strongest winds. The wind observed profile is underestimated in the WRF-simulated winds at all levels, but the biases decrease with height and the shape (positively curved) in well captured.

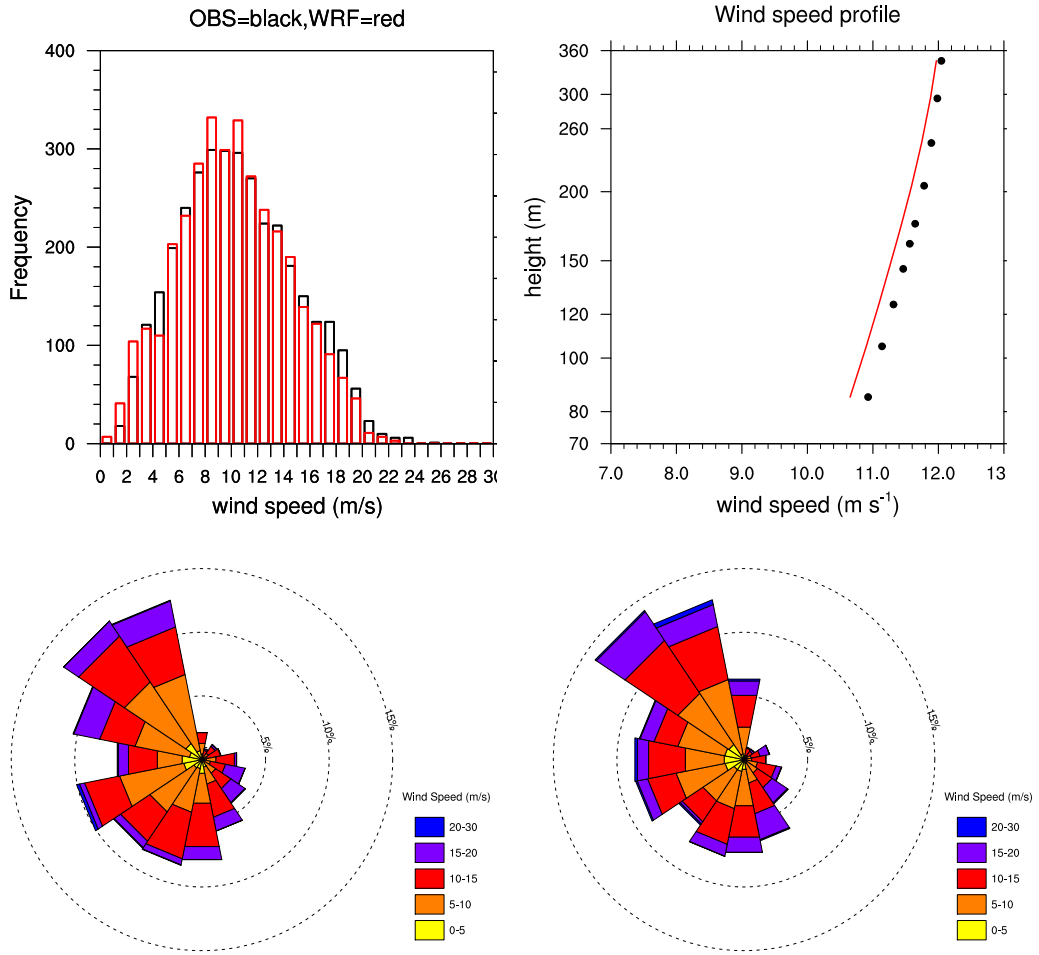

Figure 24: Wind speed distribution at 105 m (top left; OBS=black lines, WRF=red lines), mean wind speed profile (top right; OBS=black dots, WRF=red line) and wind roses for Siri at 105 m (WRF=bottom left, OBS=bottom right).

Horns Rev II

The measurements at this site come from a wind lidar, which was placed on the transformer/platform of the Horns Rev II wind farm. The winds at Horns Rev II mainly come from the west sectors (Figure 25). Therefore, the wind speeds measured at the platform are affected by the wake of the wind farm in almost every west-like wind sector.

The WRF-simulated winds underestimate the wind speed measured at Horns Rev II at all levels below 200 m. The mean relative error at 105 m is 3.6%. Biases are 0.55 m s^{-1} at 66 m and decrease with height to virtually no bias between 226–286 m. This pattern is consistent with observations being influenced by the wind farm wake at levels close to hub height of 70 m AMSL.

The wind farm was inaugurated in September 2009. Therefore, only part of the data record is affected by wakes. Comparison of the winds for the short period before the installation of the wind farm provides errors of the order of 0.3% throughout the layer from 66–286 m.

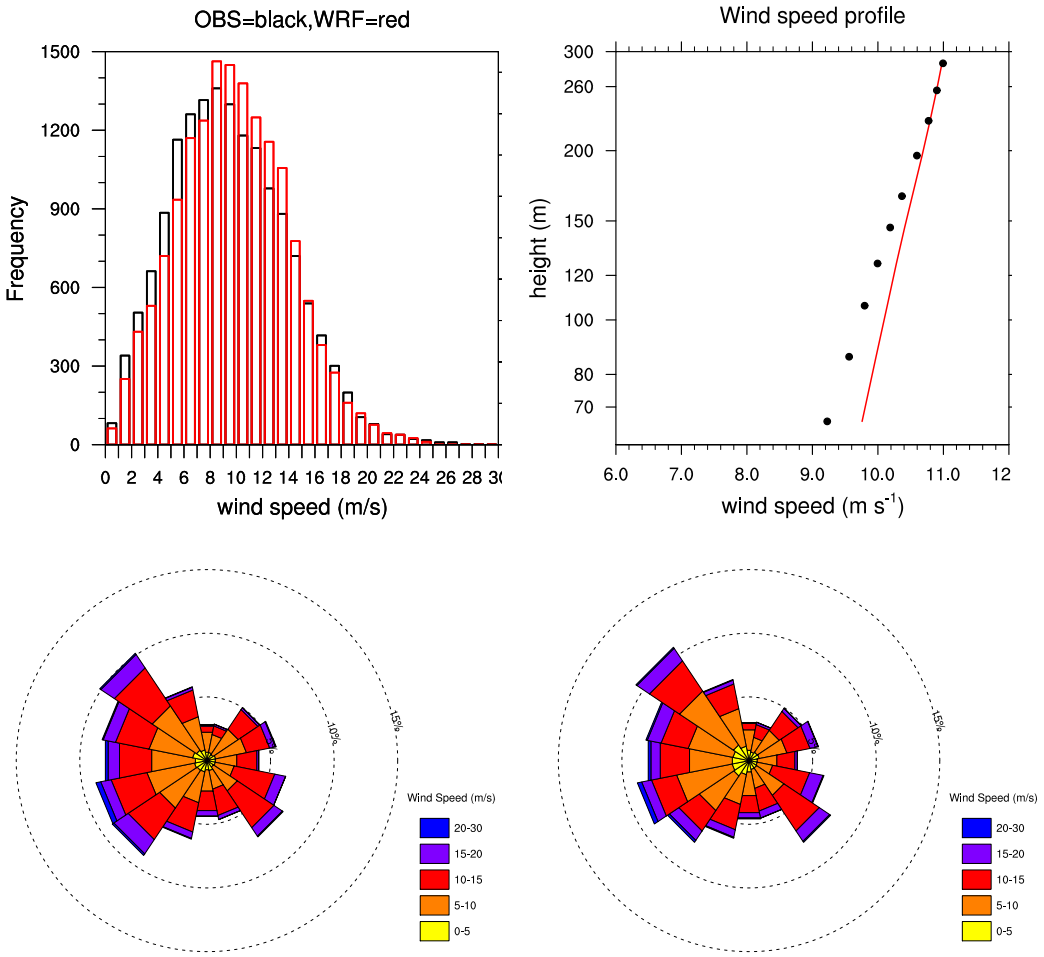

Figure 25: Wind speed distribution at 106 m (top left; OBS=black lines, WRF=red lines), mean wind speed profile (top right; OBS=black dots, WRF=red line) and wind roses for Horns Rev II at 106 m (WRF=bottom left, OBS=bottom right).

Høvsøre

The winds from observations and model simulations are compared for Høvsøre in Figure 26. The correspondence between the observed and WRF-simulated wind climatology is excellent for this site. The mean error is only -1.3% at 100 m. Bias are negative at all levels except at 10 m. Even the change in wind shear expected from the internal boundary layer created by the coastline about 2 km away is present in the WRF-simulated winds.

The wind speed distributions show similar behavior to other sites in this study, with both less low and high winds in the WRF-derived winds compared to the observed wind climatology. The wind roses are indeed very close between the two climatologies but the WRF-simulated winds are more westerly than those observed.

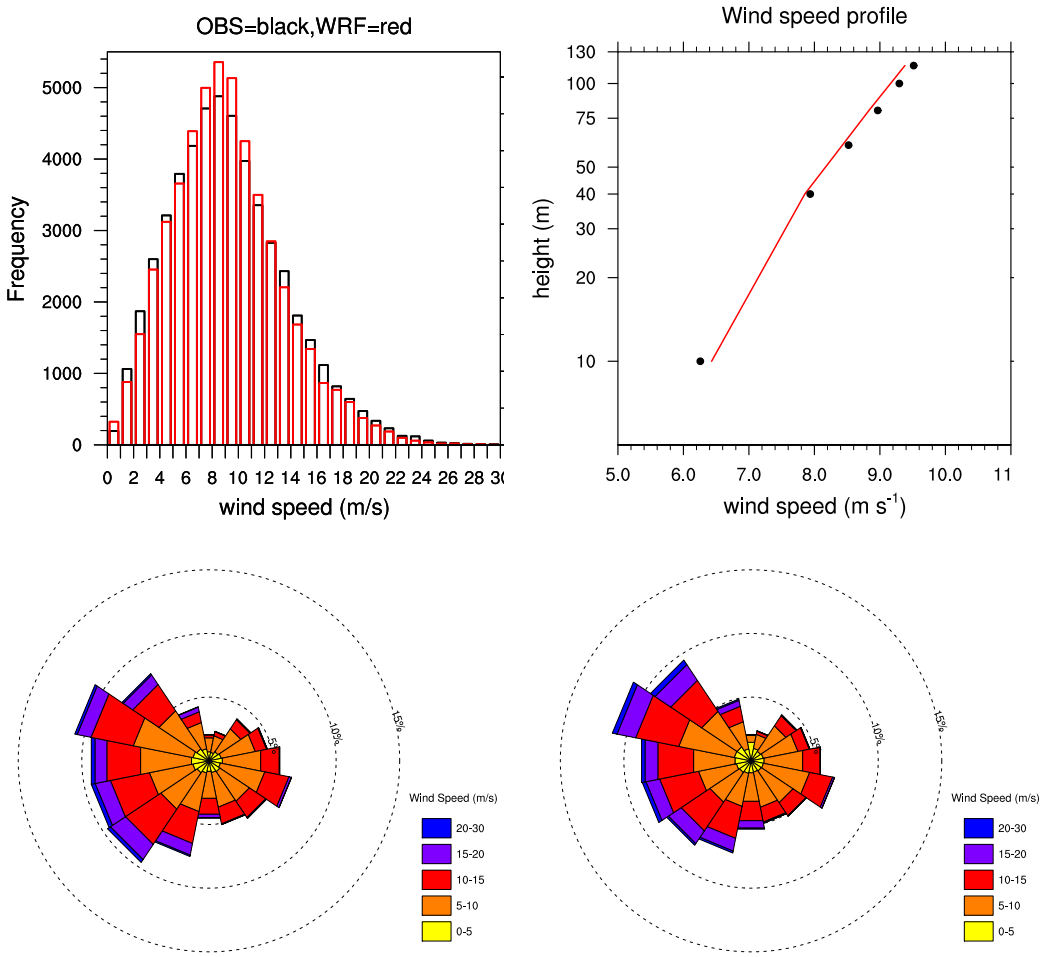

Figure 26: Wind speed distribution at 100 m (top left; OBS=black lines, WRF=red lines), mean wind speed profile (top right; OBS=black dots, WRF=red line) and wind roses for Høvsøre at 100 m (WRF=bottom left, OBS=bottom right).

5.3 Sensitivity to PBL scheme

The control experiment was repeated using the YSU2 parameterization in experiment ERA-YSU2. Annual-mean wind speeds at the sites in Table 3 for this simulation are compared to those from the ERA-HRSST (that uses the MYJ scheme) in Table 4. For the offshore sites there is very little difference between the wind speeds derived from the ERA-HRSST simulation and that from the ERA-YSU2 WRF simulation. The mean absolute bias for the offshore sites is slightly lower in the ERA-HRSST (3.12%) than in the ERA-YSU2 (3.54%). At the land sites the mean absolute bias is virtually undistinguishable from each other. But at Ryningsnäs the error is reduced from 21.2% to 17.58%. Therefore, it is not possible to give a recommendation on what scheme to use for this wind climate regime in the basis of mean-annual wind speeds simulated only.

Table 4: Comparison of the mean biases from observations in the annual-mean wind speed between winds derived from the ERA-HRSST and ERA-YSU2 simulations. Periods and heights are the same as those in Table 3.

Site	height (m)	ERA-HRSST Error (%)	ERA-YSU2 Error (%)
FINO1	90	0.96	0.85
FINO2	90	-1.69	-2.54
Horns Rev I (M7)	70	-0.32	0.11
Lillegrund	65	8.20	8.47
Östergarnsholm	30	3.86	5.04
Siri	105	-3.24	-4.19
Horns Rev II	106	3.59	3.59
CS (Öland)	50	-6.51	-5.62
Absolute error (offshore):		3.12	3.54
Østeril syd	44	13.18	14.94
Østeril vest	44	8.82	10.13
Høvsøre	100	-1.30	-0.76
Risø	76	1.37	1.37
Risø	125	2.40	2.83
Ryningsnäs	98	21.16	17.58
Absolute error (land):		8.04	7.93

5.4 Generalized wind climatologies

In this section we use the generalized wind climatologies derived from several surface stations around Denmark. Data for most of the stations are given at a height of 10 meters and for the period 1987–96 (Mortensen et al., 1999). This period does not coincide with that of the WRF simulations, however, the intent of this comparison is not to evaluate the absolute value of the WRF-derived wind atlas, but to evaluate the value of the generalization method. The sites are spread across Denmark and the danish island of Bornholm in the Baltic Sea. The generalization of the observed wind climatology was done using the linear microscale model WAsP. Generalized winds are shown in Table 5 for a height of 100 m and a uniform roughness of 3 cm. The generalization of the winds derived from the WRF simulations follows the procedure outlined in Section 3.4. Surface roughness lengths from summer and winter are used separately and the water roughness is derived from u_* in the model using Charnock's relation.

Table 5: Comparison of raw and generalized annual-average wind speeds across Denmark in the observations and the ERA-HRSST simulation. The "L" or "O" in the station name indicates whether the generalized WRF wind climatology came from a grid point over land or ocean, respectively. The generalization is done for a height of 100 m and a roughness of 3 cm.

	Station	height (m)	lat (°N)	lon (°E)	U OBS ($m\,s^{-1}$)	U WRF ($m\,s^{-1}$)	U OBS Gen ($m\,s^{-1}$)	U WRF Gen ($m\,s^{-1}$)
1	Risø (L)	70	55.69	12.09	8.01	6.79	7.58	8.72
2	Sprogø (O)	70	55.55	10.94	8.24	8.41	7.84	7.77
3	Beldringe (L)	10	55.29	10.20	5.31	5.03	8.56	8.57
4	Gniben (O)	10	56.01	11.29	7.28	7.60	7.89	8.10
5	Kastrup (L)	9	55.62	12.67	5.67	4.31	8.29	8.29
6	Mejrup (L)	10	56.38	8.67	5.18	5.08	9.07	8.76
7	Sjælsmark (L)	10	55.88	12.41	3.96	4.31	7.19	8.21
8	Abed (L)	10	54.82	11.33	4.76	5.13	8.18	8.61
9	Altesdgård (L)	10	55.40	11.67	4.68	4.97	8.40	8.66
10	Bønsvig (O)	10	55.10	12.17	4.60	5.93	7.33	7.95
11	Børglum (L)	31.5	57.35	9.81	6.61	5.87	9.18	8.75
12	Dueodde (L)	10	55.00	15.07	5.22	5.78	8.75	8.61
13	Gedser (O)	12	54.56	11.97	7.22	7.39	8.16	8.23
14	Skjem (L)	24.1	55.94	8.45	6.20	6.18	8.68	8.66
15	Klemensk (L)	10	55.18	14.80	4.98	5.62	8.71	8.97
16	Tystofte (L)	39.3	55.24	11.33	6.46	6.77	8.19	8.35
Mean absolute error (%):						9.2		4.1

Figure 27 shows that the relative errors between the raw winds in the observations and in the model simulations vary between 0 and 29% and the averaged mean error is 9.2%. The errors in the generalized annual mean winds (at 100 m and over a homogeneous surface of 3 cm roughness) between the simulated and observed winds are lower than 15% in all sites, with most sites showing errors lower than 5%. The averaged mean absolute error is only 4.1% despite the differences in the periods used for averaging between the observations and the model simulations.

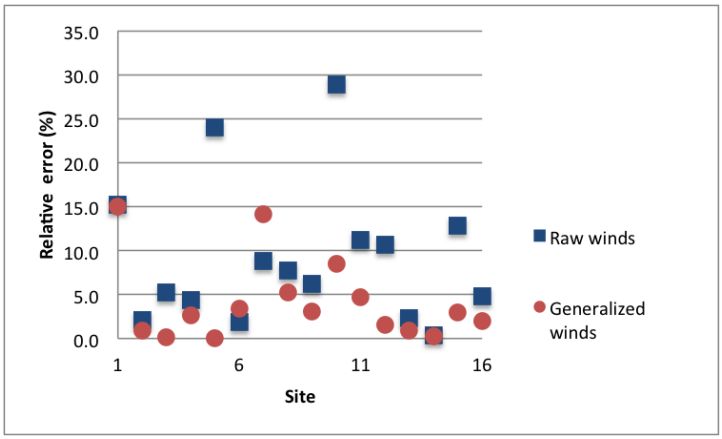

Figure 27: Comparison of absolute errors (%) between raw and simulated winds and generalized observed and simuated winds using the ERA-HRSST WRF simulation for all the sites in the Danish Wind Atlas (Mortensen et al., 1999). The site numbers correspond to those in Table 5.

6 The wind atlas

Here we introduce graphical representations of the wind climatology and boundary layer state extracted from the control WRF simulation (ERA-HRSST in Table 2).

6.1 Mean annual wind speed

Maps of annual mean wind speed for the period 2006–2011 and long-term corrected to the reference period 1999–2011 are presented in Figures 28 and 29, respectively for 100 m AGL. Vertical interpolation using a cubic spline between model levels has been used to compute wind speeds at these levels. These are derived from the control simulation described in section 2.2. The long-term corrected field has been computed using the technique described in section 3.1.

6.2 Generalized wind speed

Figure 30 shows the generalized wind speeds derived from the WRF model output at a height of 100 m and a uniform flat surface with surface roughness of 0.0002 m (i.e., the standard WAsP water surface roughness). This generalized wind was computed using the procedure described in Section 3.4. Note the overall increase in wind speeds compared to the simple time-average wind speeds in Figure 28. This is a consequence of the generalization to a uniform surface roughness 0.0002 m while WRF surface roughness, computed through the Charnook's relation, are often larger than this value. In addition, gradients in wind speed are less pronounced in the generalized wind speeds.

6.3 Weibull distribution parameters

Using the method described in section 3.2, we calculated A and k for the control simulation covering the period 2006–2011. Geographic maps of these two parameters are shown in Figure 31. Note that the values of A and k are quite sensitive to the method used for fitting these parameters. By the method adopted here, we make sure that when computing the mean power density, the same values as those computed directly from the data are obtained.

The values of A vary between $\sim$8 m s^{-1} along most coastlines, to over 11 m s^{-1} in the North Sea. The values of k are above 2.4 in the South Baltic, but $k < 2.1$ can be found along the Swedish and Danish west coasts. The shadow of the land gives higher values of k, i.e., more "peaky" wind speed distributions.

6.4 Interannual variability

Maps of the mean annual wind speed for all years in the period 2006–2011 are presented in Figure 32. It is obvious that this region experiences considerable differences in wind speed from year to year: with the largest wind speeds in 2007 and the lowest in 2006. Variability is not always in phase in the North Sea and the South Baltic. The mean wind speed in years 2009 and 2010 (Figure 32 (d) and (e)) is similar in the South Baltic Sea, while the mean wind speed in years 2006 and 2009 (Figure 32 (a) and (d)) is similar in the North Sea.

Maps of the inter-annual variability as represented by the standard deviation of the mean annual wind speed are presented in Figure 33 both for the control simulation (2006–2011) and for the reference simulation (1999–2011). While some patterns are consistent (e.g., in the southern Baltic), the strongest variability is found in the North Sea and along the Norwegian coast. However, the period is still too short to estimate the real inter-annual variability in this region.

6.5 Wind shear exponent

The time-average (2006–2011) of the wind shear exponent, α, at 100 m as defined in section 3.3 is presented in Figure 34. Values of α vary from 0.05 in the north eastern part of the Baltic Sea to 0.25 or larger in the shadow from land in the direction downstream from the dominant flow. The largest values along the shadow of land are partly a consequence of the internal boundary layer being advected over the adjacent water. However, as seen in Figures 14 and 16, the frequency distributions of α are very non-gaussian and thus their mean not a very representative parameter.

6.6 Obukhov length

The frequency of occurrence of various stability classes in the PBL according to its Obukhov length is shown in Figure 35. The stability classes used are: unstable ($1/L < -0.005\,\mathrm{m}^{-1}$), neutral ($-0.005\,\mathrm{m}^{-1} < 1/L < 0.005\,\mathrm{m}^{-1}$), stable ($0.005\,\mathrm{m}^{-1} < 1/L < 0.02\,\mathrm{m}^{-1}$), and very stable ($1/L > 0.02\,\mathrm{m}^{-1}$). According to these maps the most common stability situation in the North and Baltic Sea is unstable. The range for neutral conditions was taken from that used from VKT and it is too restrictive. The range of $-0.001\,\mathrm{m}^{-1} < 1/L < 0.001\,\mathrm{m}^{-1}$ is most commonly used and will make these maps more compatible with the ones derived from the vertical potential temperature gradient.

Very stable and stable conditions rarely occur over the sea based on this criteria. These conditions are more dominant along the coast during the examined period. The most unstable cases occur over the sea, especially in the north of Jutland and in the east Baltic Sea.

6.7 Static stability

The frequency of occurrence of various stability classes in the PBL according to its static stability is shown in Figure 36. The classes used are: unstable ($\partial\theta/\partial z < -0.2\,\mathrm{K}/100\,\mathrm{m}$), neutral ($-0.2\,\mathrm{K}/100\,\mathrm{m} < \partial\theta/\partial z < 0.2\,\mathrm{K}/100\,\mathrm{m}$), stable ($0.2\,\mathrm{K}/100\,\mathrm{m} < \partial\theta/\partial z < 0.5\,\mathrm{K}/100\,\mathrm{m}$), and very stable ($\partial\theta/\partial z > 0.5\,\mathrm{K}/100\,\mathrm{m}$) as defined by the vertical gradient of potential temperature between 14 and 100 m.

The comparison of the stability classes based on the Obukhov Length L (Figure 35) versus those from the vertical gradient of potential temperature (Figure 36) shows that the spatial distribution of the unstable class is similar, but that from the vertical gradient of potential temperature shows less unstable cases. More dominant is the occurrence of the neutral class, especially over the North Sea, when analyzing the vertical gradient of potential temperature. Stable cases rarely occur. The very stable class is mostly spread over the Baltic Sea between Germany, Denmark and Sweden, as well as along the coast.

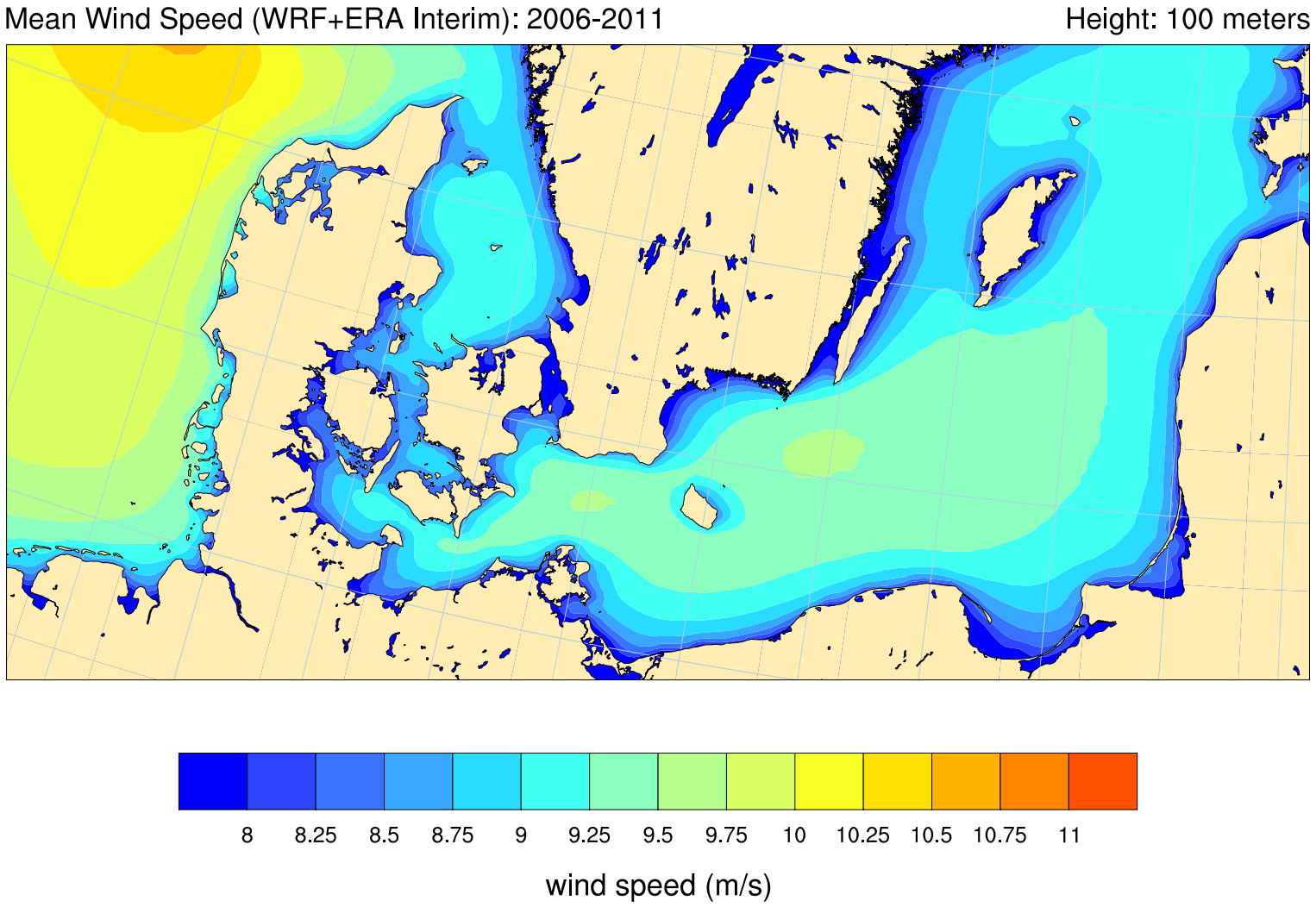

Figure 28: Time-averaged wind speed ($m\,s^{-1}$) simulated by WRF for the period 2006–2011 and interpolated to the level of 100 m.

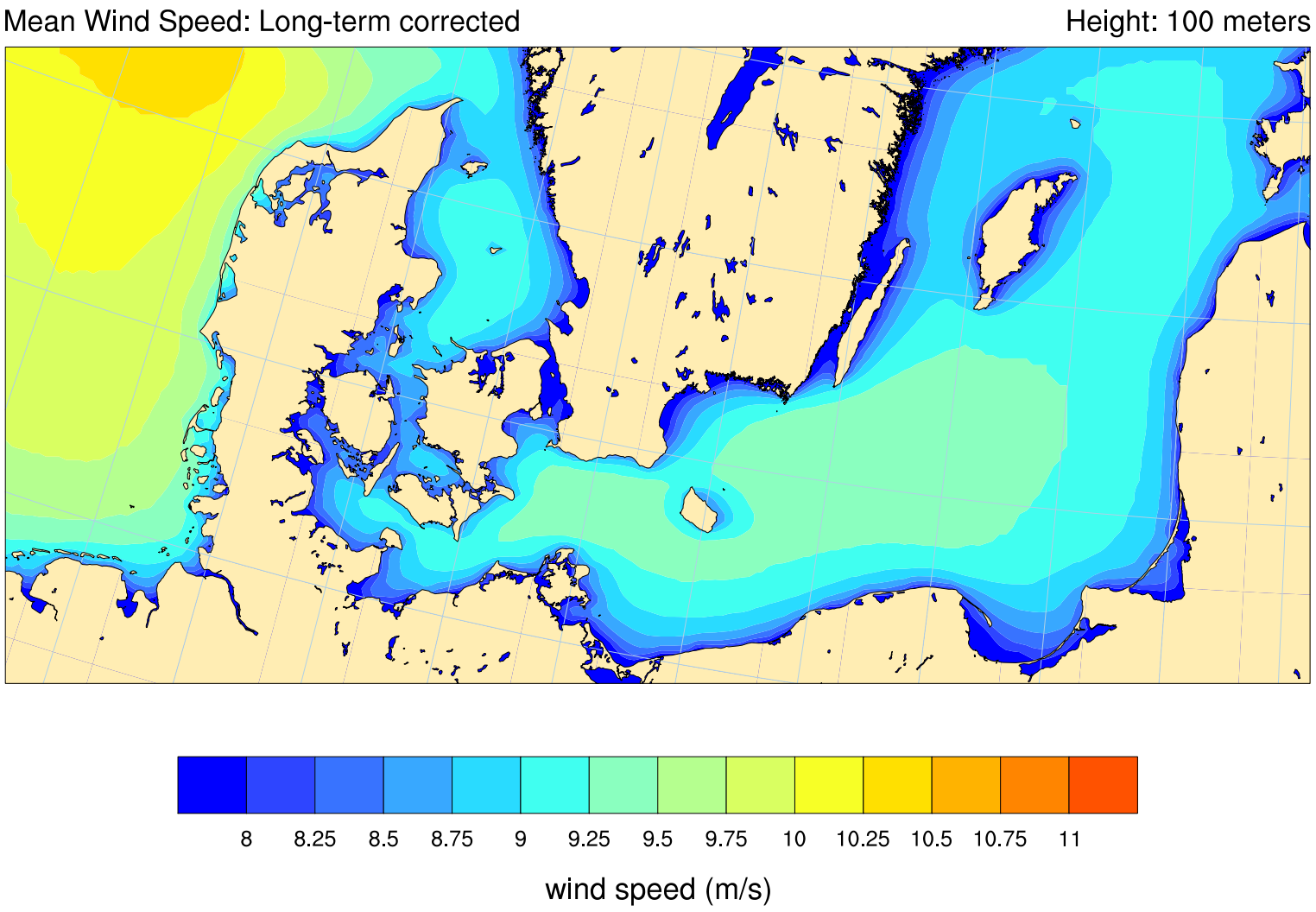

Figure 29: Long-term corrected (reference period 1999–2011) wind speed ($m\,s^{-1}$) at 100 m simulated by WRF.

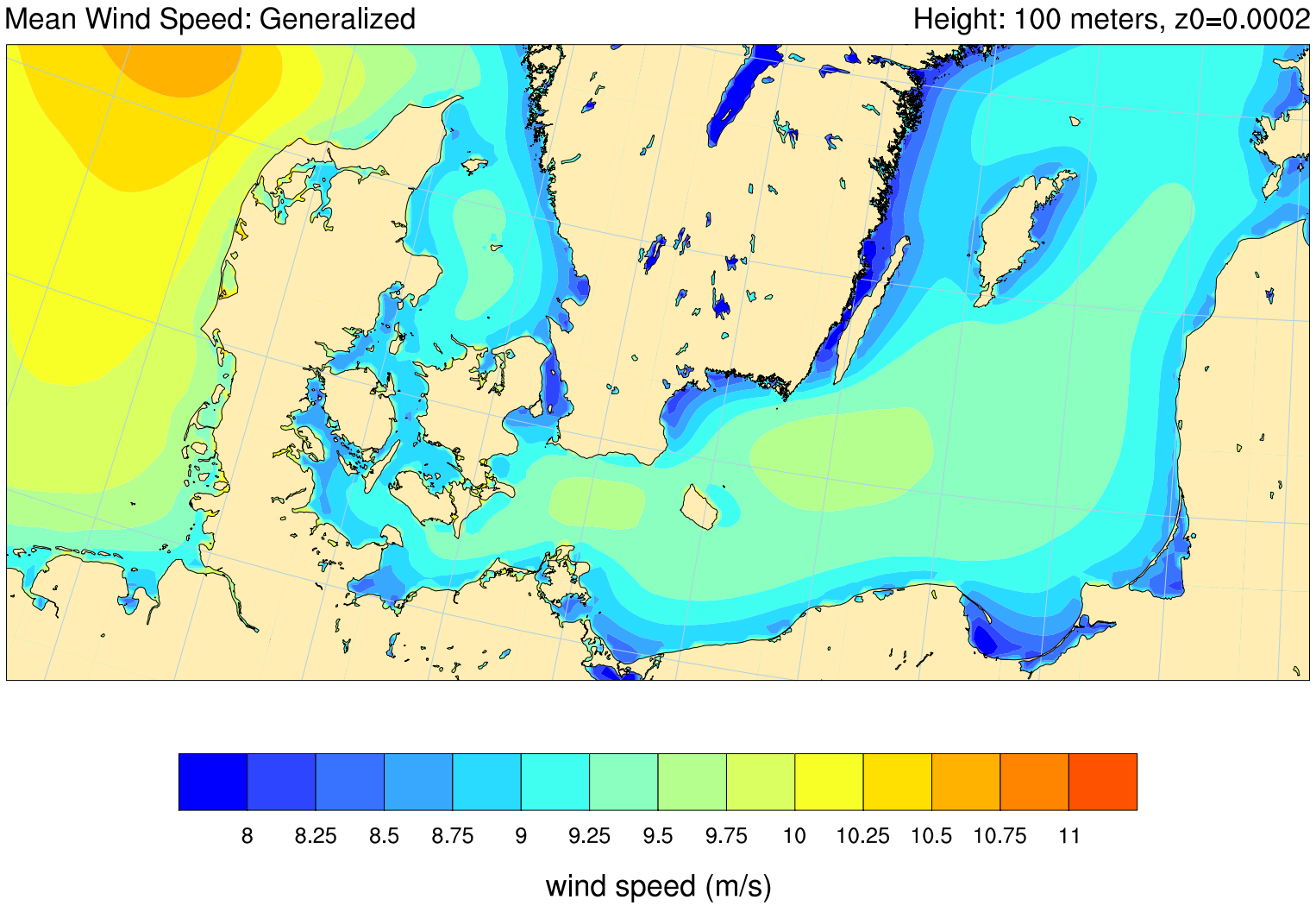

Figure 30: Time-averaged (2006–2011) generalized wind speed ($m\,s^{-1}$) at 100 m over a uniform surface of 0.0002 m roughness simulated by WRF.

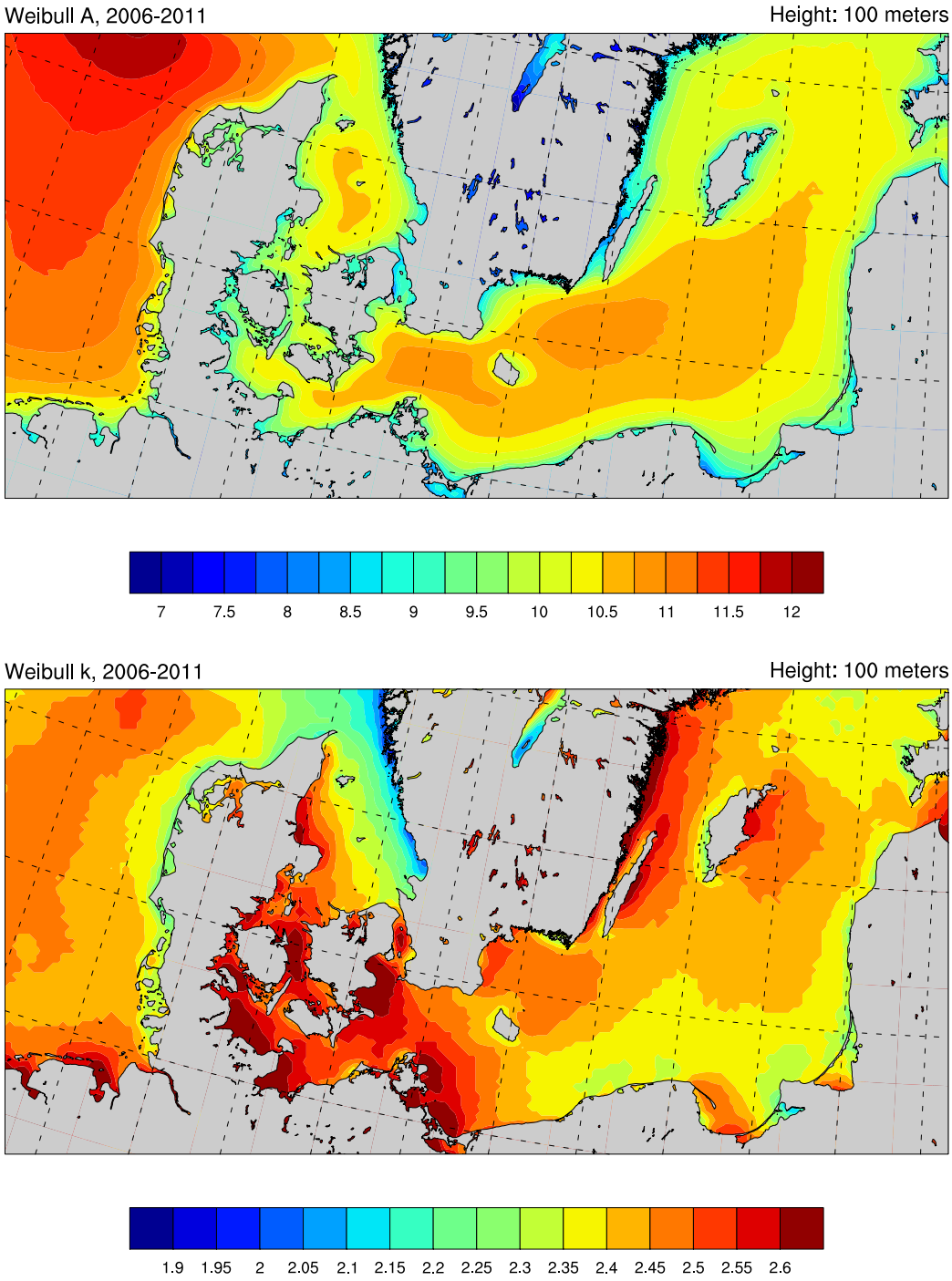

Figure 31: Weibull A ($\mathrm{m\,s^{-1}}$) and k parameters computed from the wind speed time series at 100 meters in the control simulation (2006–2011).

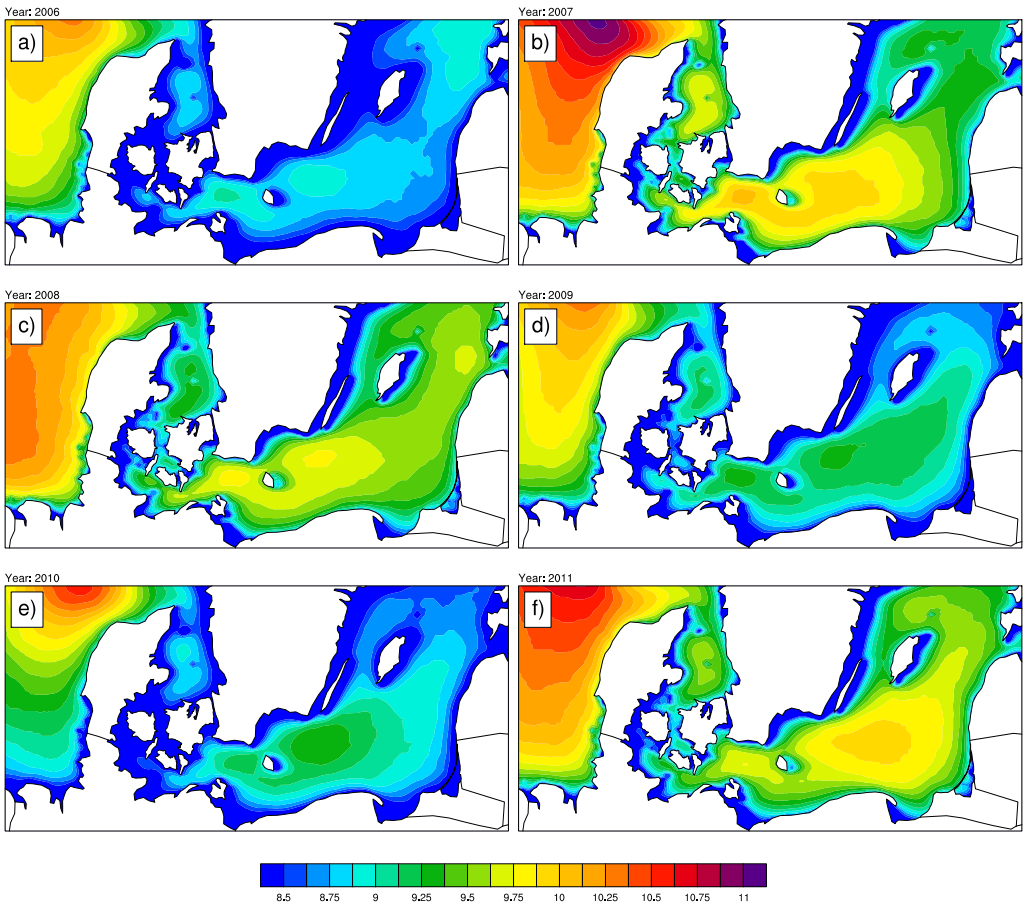

Figure 32: Annual mean wind speed ($\mathrm{m\,s^{-1}}$) at 100 m during: (a) 2006, (b) 2007, (c) 2008, (d) 2009, (e) 2010, and (f) 2011.

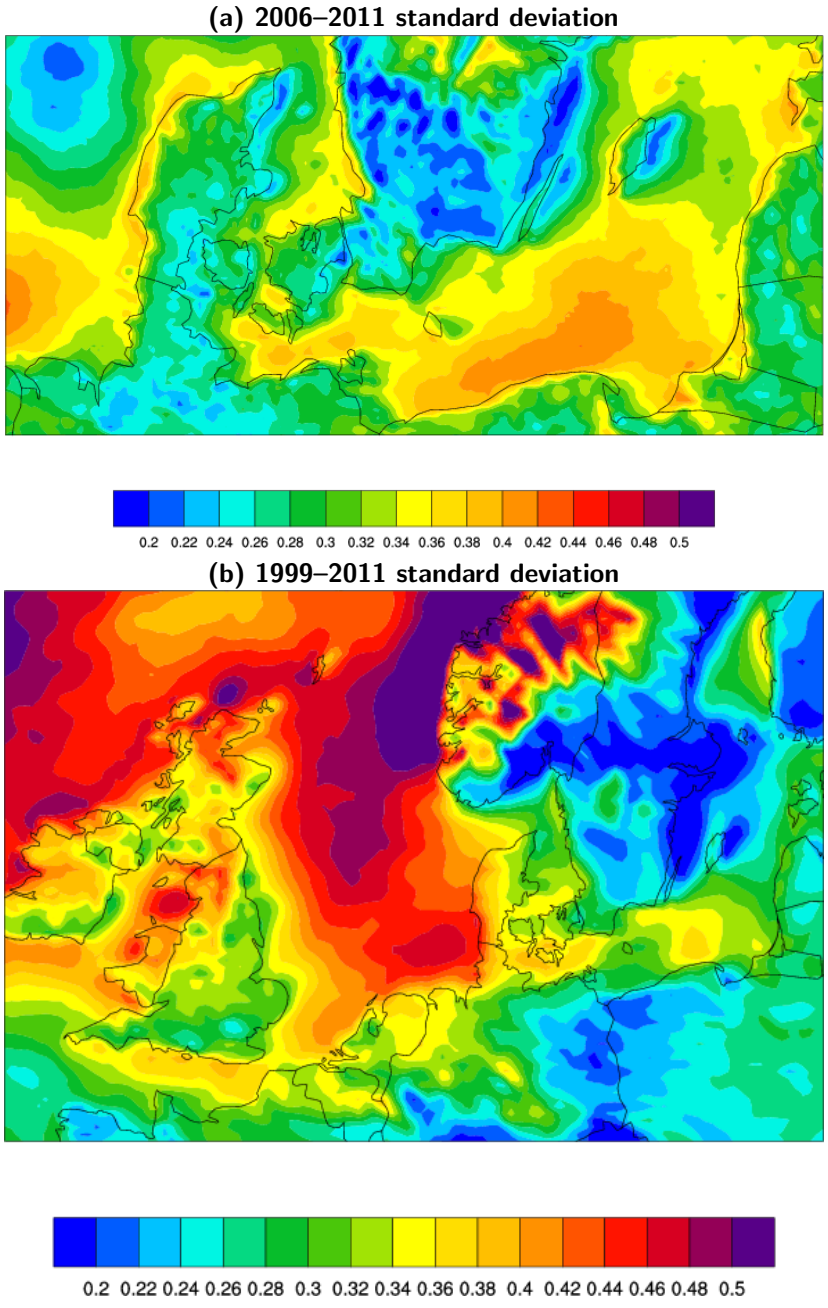

Figure 33: Standard deviation ($m\,s^{-1}$) in the mean annual wind speed at 100 m in: (a) control simulation (2006–2011), (b) reference simulation (1999–2011).

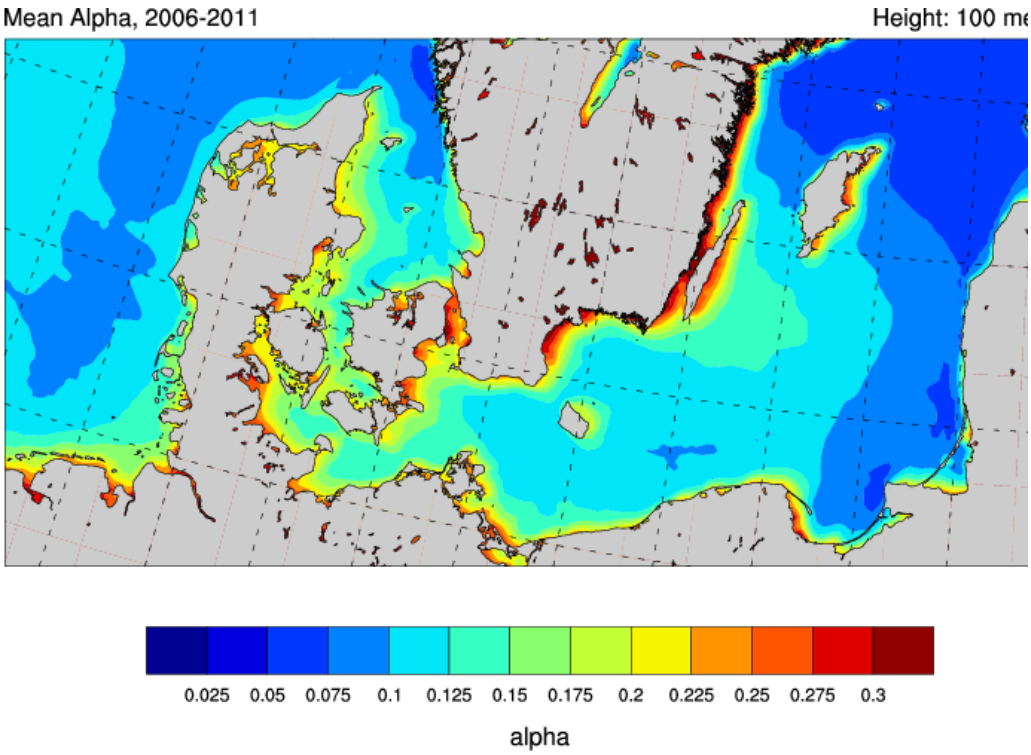

Figure 34: Time-averaged mean (2006–2011) of the wind shear exponent α at 100 m.

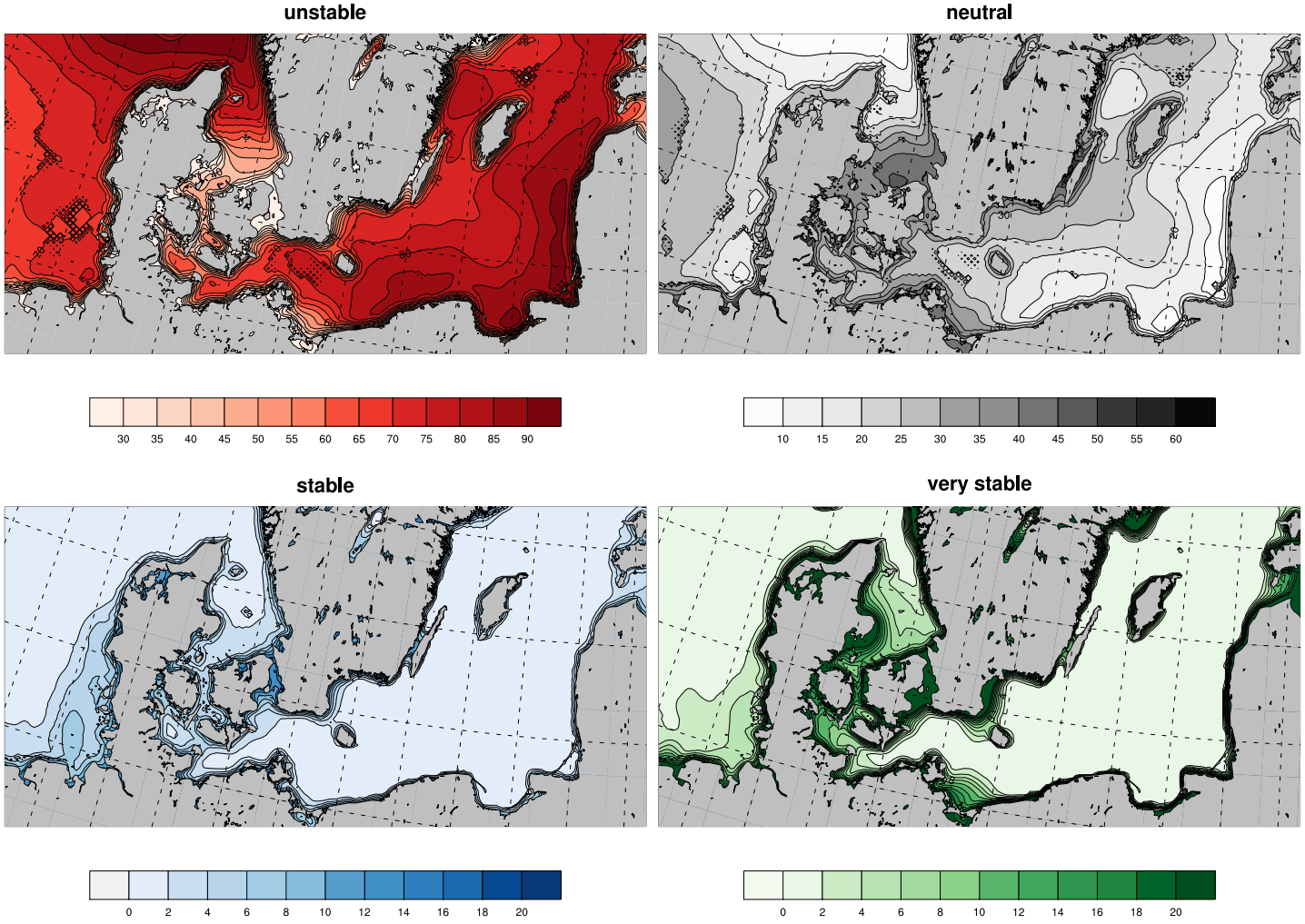

Figure 35: Frequency of occurrence (%) of various stability classes in the 2006–2011 period as defined by the Obukhov length L at the surface: (a) unstable ($1/L < -0.005\,\mathrm{m}^{-1}$), (b) neutral ($-0.005\,\mathrm{m}^{-1} < 1/L < 0.005\,\mathrm{m}^{-1}$), (c) stable ($0.005\,\mathrm{m}^{-1} < 1/L < 0.02\,\mathrm{m}^{-1}$), and (d) very stable ($1/L > 0.02\,\mathrm{m}^{-1}$) .

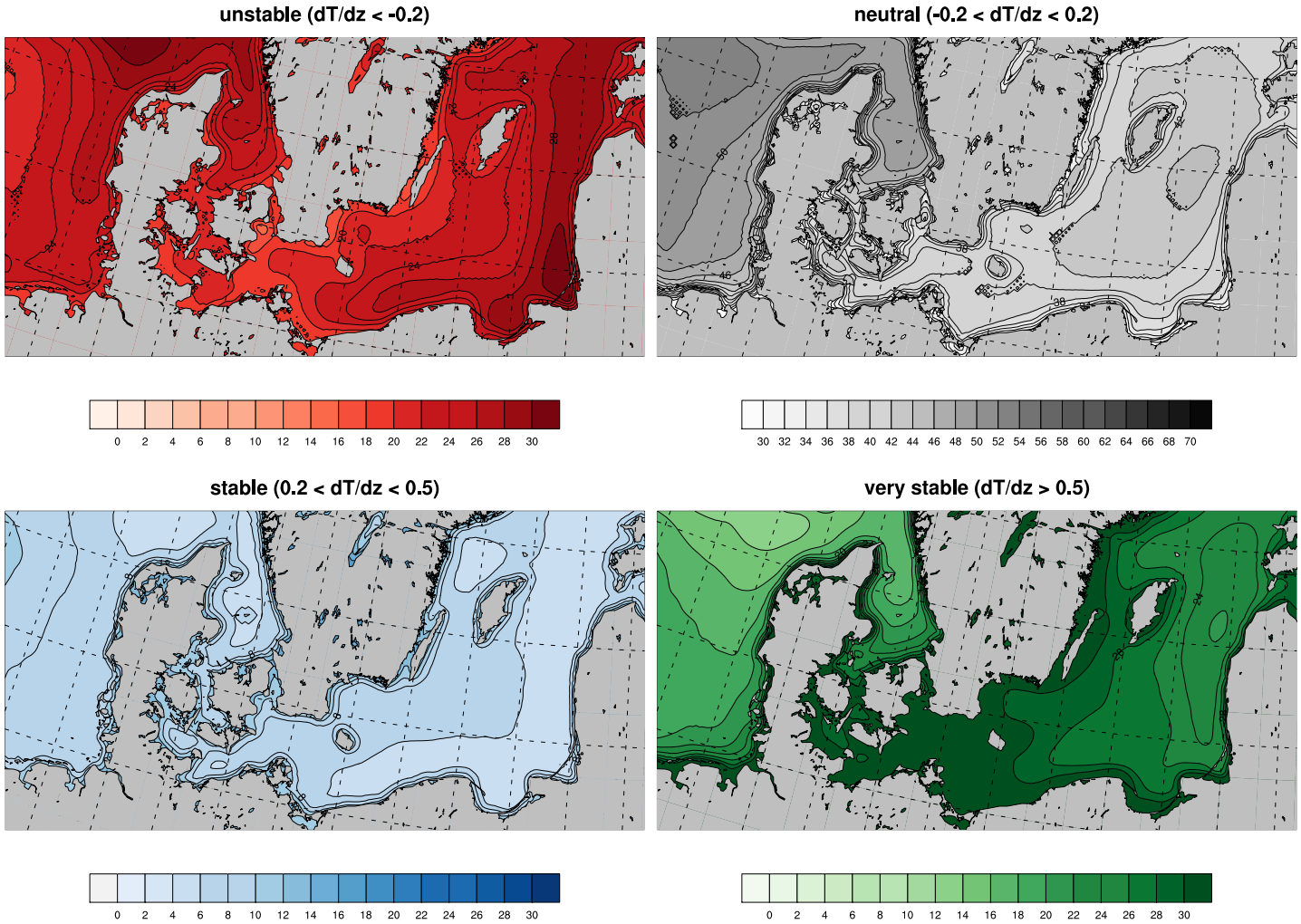

Figure 36: Frequency of occurrence (%) of various static stability classes in the 2006–2011 period: (a) unstable ($\partial\theta/\partial z < -0.2\,\mathrm{K}/100\,\mathrm{m}$), (b) neutral ($-0.2\,\mathrm{K}/100\,\mathrm{m} < \partial\theta/\partial z < 0.2\,\mathrm{K}/100\,\mathrm{m}$), (c) stable ($0.2\,\mathrm{K}/100\,\mathrm{m} < \partial\theta/\partial z < 0.5\,\mathrm{K}/100\,\mathrm{m}$), and (d) very stable ($\partial\theta/\partial z > 0.5\,\mathrm{K}/100\,\mathrm{m}$) as defined by the vertical gradient of potential temperature between 14 and 100 m.

7 Summary and conclusions

This report outlines the steps taken to create a numerical wind atlas for the South Baltic under the EU project NORSEWInD. The atlas was created from wind time series from long-term simulations with the mesoscale numerical model WRF.

As a way of finding the best model configuration for creating numerical wind atlases a series of sensitivity simulations were run for a year. The runs explore the wind sensitivity to driving reanalysis, sea surface temperatures, nudging parameters and re-initialization frequency, vertical resolution, and PBL scheme. Of all these variables, only the length of the spin-up period and the PBL scheme show significant differences (i.e. $> 5\%$ differences in the annual mean wind speed). However, the differences in mean wind speed due to the different PBL schemes are smaller than the relative errors to the observations. Therefore, it is not possible to give a recommendation on what scheme to use for this wind climate regime in the basis of only the mean-annual wind speed simulated by these two parameterizations.

The lack of sensitivity in annual mean wind speed of the model simulations to many model and setup parameters applies only to the mean wind speed. Parameters such as the shear or Obukhov length can vary substantially due to changes in PBL scheme. In addition, the simulated distributions in wind speed can also vary considerably. These sensitivities are not explored in this report but were already reported elsewhere (Hu et al., 2010; Draxl et al., 2012).

The comparison of the model results against wind measurements offshore shows excellent results for most sites. The mean absolute error over 8 sites in the North and Baltic Seas is 2.9%. Among these sites the largest relative errors are found for sites which are contaminated by the presence of a wind farm or are close to the coast. Over land the errors are larger (mean absolute error of about 8%) especially over forest or for sites with large changes in surface roughness. Over forest, the wind simulated by WRF overestimates the observed wind speed. This error can be partly compensated by introducing a displacement height of the order of the forest height in the interpolation of the model winds. Also, the roughness length for forest used in WRF is only 0.5 m which severely underestimates the values estimated at forest sites in Sweden. This issue is currently being explored in a separate set of model sensitivities.

The added value of generalizing model simulated wind climatologies is demonstrated by the comparison of the WRF model wind climatologies to generalized wind climates over land which are part of the Danish Wind Atlas (Mortensen et al., 1999). When "raw" wind time series are compared the mean absolute error is 9.2%. The comparison of the generalized wind climatologies both from the observations (using WAsP) and the simulated winds brings down the error to 4.1%. The periods of the observations and the model simulations do not coincide. However, the intent of this comparison is not to evaluate the absolute value of the WRF-derived wind atlas, but to evaluate the value of the generalization method.

References

Badger, J., H. Frank, G. Giebel, and A. N. Hahmann, 2013: Wind climate estimation based on mesoscale and microscale modelling: statistical-dynamical downscaling for wind energy applications. *J. Appl. Meteor. Climatol.*, **in preparation**.

Dee, D. P., et al., 2011: The ERA-Interim reanalysis: configuration and performance of the data assimilation system. *Quart. J. Roy. Meteor. Soc.*, **137 (656, Part A)**, 553–597, doi: 10.1002/qj.828.

Draxl, C., A. N. Hahmann, A. Peña, and G. Giebel, 2012: Evaluating winds and vertical wind shear from WRF model forecasts using seven PBL schemes. *Wind Energy*, **in Press**.

Gemmill, W., B. Katz, and X. Li, 2007: Daily real-time global sea surface temperature - high resolution analysis at NOAA/NCEP. Office note nr. 260, 39 pp, NOAA/NWS/NCEP/MMAB.

Gryning, S. E., E. Batchvarova, B. Brümmer, H. Jørgensen, and S. Larsen, 2007: On the extension of the wind profile over homogeneous terrain beyond the surface layer. *Bound.-Layer Meteor.*, **124**, 251–268.

Hagemann, K., 2008: Mesoscale wind atlas of South Africa. Ph.D. thesis, University of Cape Town, Cape Town, South Africa.

Hahmann, A. N. and A. Peña, 2010: Validation of boundary-layer winds from WRF mesoscale forecasts over Denmark. *European Wind Energy Conference and Exhibition*, Warsaw, Poland.

Hahmann, A. N., D. Rostkier-Edelstein, T. T. Warner, F. Vandenberghe, Y. Liu, R. Babarsky, and S. P. Swerdlin, 2010: A reanalysis system for the generation of mesoscale climatographies. *Journal of Applied Meteorology and Climatology*, **49 (5)**, 954–972, doi:DOI 10.1175/2009JAMC2351.1.

Hong, S.-Y., Y. Noh, and Dudhia., 2006: A new vertical diffusion package with an explicit treatment of entrainment processes. *Mon. Wea. Rev.*, **134**, 2318–2341.

Horvath, K., D. Koracin, R. Vellore, J. Jiang, and R. Belu, 2012: Sub-kilometer dynamical downscaling of near-surface winds in complex terrain using WRF and MM5 mesoscale models. *Journal of Geophysical Research-Atmospheres*, **117**, D11 111, doi:DOI 10.1029/2012JD017432.

Hu, X.-M., J. W. Nielsen-Gammon, and F. Zhang, 2010: Evaluation of three planetary boundary layer schemes in the WRF model. *Journal of Applied Meteorology and Climatology*, **49 (9)**, 1831–1844, doi:10.1175/2010JAMC2432.1.

Kanamitsu, M., W. Ebisuzaki, J. Woollen, S. K. Yang, J. J. Hnilo, M. Fiorino, and G. L. Potter, 2002: NCEP-DOE AMIP-II reanalysis (R-2). *Bull. Amer. Meteor. Soc.*, **83**, 1631–1643.

Larsén, X. G., J. Badger, A. N. Hahmann, and N. Mortensen, 2012: The selective dynamical downscaling method for extreme wind atlases. *Wind Energy*, **In press**.

Larsén, X. G., S. Larsen, and A. N. Hahmann, 2012: Origin of the waves in A case-study of mesoscale spectra of wind and temperature, observed and simulated': Lee waves from the Norwegian mountains. *Quart. J. Roy. Meteor. Soc.*, **138 (662, Part A)**, 274–279, doi:10.1002/qj.916.

Mellor, G. L. and T. Yamada, 1982: Development of a turbulence closure model for geophysical fluid problems. *Rev. Geophys. and Space Phys.*, **20**, 851–875.

Miguez-Macho, G., G. Stenchikov, and A. Robock, 2004: Spectral nudging to eliminate the effects of domain position and geometry in regional climate model simulations. *Journal of Geophysical Research-Atmospheres*, **109 (D13)**, D13 104, doi:DOI 10.1029/2003JD004495.

Mortensen, N. G., O. Rathmann, L. Landberg, G. Jensen, and E. Petersen, 1999: Wind atlas analysis of 26 Danish stations (1987–96). Tech. Rep. Risø-R-1092, Risø National Laboratory (unpublished).

Peña, A. and A. N. Hahmann, 2012: Atmospheric stability and turbulence fluxes at Horns Rev — An intercomparison of sonic, bulk and WRF model data. *Wind Energy*, doi:DOI: 10.1002/we.500.

Peña, A., A. N. Hahmann, C. B. Hasager, F. Bingöl, I. Karagali, J. Badger, M. Badger, and N.-E. Clausen, 2011: South Baltic Wind Atlas. South Baltic Offshore Wind Energy Regions Project. ISBN: 978-87-550-3899-8 Risø-R-1775(EN), Risø DTU.

Peña, A., C. B. Hasager, S.-E. Gryning, M. Courtney, I. Antoniou, and T. Mikkelsen, 2009: Offshore wind profiling using light detection and ranging measurements. *Wind Energy*, **12**, 105–124.

Peña, A., T. Mikkelsen, S.-E. Gryning, C. Hasager, A. Hahmann, M. Badger, I. Karagali, and M. Courtney, 2012: *Offshore vertical wind shear: Final report on NORSEWInD's work task 3.1*. DTU Wind Energy.

Rife, D. L., E. Vanvyve, J. O. Pinto, A. J. Monaghan, and C. A. Davis, 2012: Selecting representative days for more efficient dynamical climate downscaling: Application to wind energy. *J. Appl. Meteor. Climatol.*, **In press**.

Saha, S., et al., 2010: The NCEP Climate Forecast System Reanalysis. *Bull. Amer. Meteor. Soc.*, **91 (8)**, 1015–1057, doi:10.1175/2010BAMS3001.1.

Skamarock, W. C., et al., 2008: A Description of the Advanced Research WRF Version 3. Tech. Rep. NCAR/TN–475+STR, National Center for Atmospheric Research.

Storm, B., J. Dudhia, S. Basu, A. Swift, and I. Giammanco, 2009: Evaluation of the weather research and forecasting model on forecasting low-level jets: implications for wind energy. *Wind Energy*, **12 (1)**, 81–90.

Stull, R. B., 1988: *An Introduction to Boundary Layer Meteorology*, Atmospheric and Oceanographic Sciences Library, Vol. 13. Springer, 680 pp., iSSN 978-90-277-2769-5.

Tammelin, B., et al., 2012: Production of the finnish wind atlas. *Wind Energy*, n/a–n/a, doi:10.1002/we.517, URL `http://dx.doi.org/10.1002/we.517`.

Troen, I. and E. L. Petersen, 1989: *European Wind Atlas*. Published for the Commission of the European Communities, Directorate-General for Science, Research, and Development, Brussels, Belgium by Risø National Laboratory.

Tuller, S. E. and A. C. Brett, 1984: The characteristics of wind velocity that favor the fitting of a weibull distribution in wind-speed analysis. *J. Appl. Meteor. Climatol.*, **23 (1)**, 124–134, doi:10.1175/1520-0450(1984)0232.0.CO.

Vincent, C. L., A. N. Hahmann, and M. C. Kelly, 2012: Idealized mesoscale model simulations of open cellular convection over the sea. *Boundary-Layer Meteorology*, **142 (1)**, 103–121, doi:DOI 10.1007/s10546-011-9664-7.

Wang, W., et al., 2010: *WRF-ARW Version 3 Modeling System User's Guide*. Mesoscale & Microscale Meteorology Division, National Center for Atmospheric Research, Boulder, USA.

DTU Wind Energy
Technical University of Denmark

Frederiksborgvej 399
4000 Roskilde
Denmark
Phone +45 4677 5024

www.vindenergi.dtu.dk